

Bright and Dark Matter in Elliptical Galaxies: Mass and Velocity Distributions from Self-consistent Hydrodynamical Simulations

J. Oñorbe¹, R. Domínguez-Tenreiro¹, A. Sáiz^{1★}, and A. Serna²

¹*Departamento de Física Teórica, C-XI. Universidad Autónoma de Madrid, Madrid, E-28049, Spain*

²*Departamento de Física y A.C., Universidad Miguel Hernández, Elche, Spain*

2 December 2024

ABSTRACT

We have analysed the mass and velocity distributions of two samples of relaxed elliptical-like-objects (ELOs) identified, at $z = 0$, in a set of self-consistent hydrodynamical simulations operating in the context of a concordance cosmological model. ELOs have been identified as those virtual galaxies having a prominent, dynamically relaxed stellar spheroidal component, with no extended discs and very low gas content. Our analysis shows that they are embedded in extended, massive dark matter haloes, and they also have an extended corona of hot diffuse gas. Dark matter haloes have experienced adiabatic contraction along their assembly process. The relative ELO dark- to bright-mass content and space distributions show broken homology, and they are consistent with observational results on the dark matter fraction at the central regions, as well as on the gradients of the mass-to-light ratio profiles for boxy ellipticals, as a function of their stellar masses. These results indicate that massive ellipticals miss stars (i.e., baryons) at their central regions, as compared with less massive ones. Our simulations indicate that these missing baryons could be found beyond the virial radii as a hot, diffuse plasma. This mass homology breaking could have important implications to explain the physical origin of the Fundamental Plane relation. The projected stellar mass profiles of our virtual ellipticals can be well fit by the Sérsic (1968) formula, with shape parameters n that agree, once a stellar mass-to-light ratio independent of position is assumed, with those obtained from surface brightness profiles of ellipticals. The agreement includes the empirical correlations of n with size, luminosity and velocity dispersion. The total mass density profiles show a power-law behaviour over a large r/r_{vir} interval, consistent with data on massive lens ellipticals at shorter radii. The velocity dispersion profiles show kinematical segregation, with no systematic mass dependence (i.e., no dynamical homology breaking) and a positive anisotropy (i.e., radial orbits), roughly independent of the radial distance outside the central regions. The LOS velocity dispersion profiles are declining. These results give, for the first time from cosmological simulations, a rather detailed insight into the intrinsic mass and velocity distributions of the dark, stellar and gaseous components of virtual ellipticals. The consistency with observations strongly suggests that they could also describe important intrinsic characteristics of real ellipticals, as well as some of their properties recently inferred from observational data (for example, downsizing, the appearance of blue cores, the increase of the stellar mass contributed by the elliptical population as z decreases).

Key words: galaxies: elliptical and lenticular, cD - galaxies: haloes - galaxies: kinematics and dynamics - galaxies: structure - dark matter - hydrodynamics

1 INTRODUCTION

Among all galaxy families, elliptical galaxies (Es) are the simplest ones and those that show the most precise empirical regularities. Such as are, for example, the very similar shapes their surface brightness profiles show (i.e., the Sérsic law, Sérsic 1968), or, even more significantly if confirmed, the power-law form of their three-dimensional mass density profiles emerging from strong lensing analyses (Koopmans et al. 2006), or the relations among some of their observable parameters. The importance of these regularities lies in that they very likely encode a lot of relevant informations on the physical processes underlying the histories of the mass assembly, the rates of dissipation and the rates of star formation of elliptical galaxies.

Despite of their interest, very few is known, both from the theoretical or observational points of view, about the mass or velocity distributions of the different E mass components (stars, hot and cold gas and dark matter). There has been, nevertheless, an important recent progress on the photometric characterisation of E galaxies, and, in fact, authors now agree that the Sérsic law adequately describes the optical surface brightness profiles of most of them (Caon, Capaccioli, & D’Onofrio 1993; Trujillo, Graham, & Caon 2001; Bertin, Ciotti, & Del Principe 2002). The Sérsic law can be written

$$I^{\text{light}}(R) = I_0^{\text{light}} \exp[-b^n (R/R_e^{\text{light}})^{1/n}], \quad (1)$$

where $I^{\text{light}}(R)$ is the surface brightness at projected distance R from the E centre, R_e^{light} is the effective half-light radii, encompassing half the total galaxy luminosity, $b_n \simeq 2n - 1/3 + 0.009876/n$, and n is the Sérsic shape parameter. Putting $n = 4$ the largely used de Vaucouleurs $R^{1/4}$ law (de Vaucouleurs 1948) is recovered.

It is generally assumed that galaxies of any type are embedded in massive haloes of dark matter. However, from the observational point of view, the importance and the distribution of dark matter in E galaxies is still a matter of a living debate. Data on stellar kinematics from integrated-light spectra are very scarce beyond $2R_e^{\text{light}}$, making it difficult even to establish the presence of a dark matter halo (Kronawitter et al. 2000; Magorrian & Ballantyne 2001) through this method. Otherwise, the lack of mass tracers at larger distances that can be interpreted without any ambiguity, has historically hampered the proper mapping of the mass distribution at the outer regions of E galaxies. The situation is changing and a dramatic improvement is expected in the near future. In fact, several ongoing projects have already produced high quality data on samples of ellipticals through different methods, for example: stellar kinematics from integral-field spectroscopic measurements (SAURON, de Zeeuw et al. 2002; Cappellari et al. 2006); strong gravitational lensing (CLASS, Myers et al. 1995; LSD, Koopmans & Treu 2003, Treu & Koopmans 2004; SLACS Koopmans et al. 2006); stellar kinematics from planetary nebulae (PN.S, Douglas et al. 2002), or globular cluster (Bergond et al. 2006) observations; and X-rays (O’Sullivan & Ponman 2004a,b). In particular, the combination of high quality stellar spectroscopy and strong lensing analyses breaks the so-called mass-anisotropy degeneracy, giving strong indications that constant mass-to-light ratios can be ruled out at $> 99\%$ CL, consistent with the presence of massive and extended dark matter halos around, at least, the massive lens ellipticals analysed so far (Treu & Koopmans 2004; Koopmans et al. 2006). Moreover, these authors have also found that the dark matter and the baryons mass density profiles combine in such a way that the total mass density profiles can be fit by power-law expressions within their Einstein radii, whose slopes are consistent with isothermality. Similar conclusions on the important amounts of

* Current address: Dept. of Physics, Mahidol University, Bangkok 10400, Thailand

dark matter inside the virial radii of ellipticals have been reached from weak lensing of L_* galaxies (Guzik & Seljak 2002; Hoekstra, Yee & Gladders 2004), dynamical satellite studies (van den Bosch et al. 2004) and X-ray analyses (Humphrey et al. 2006). Other observational results or some of their interpretations, however, could suggest that the amounts of dark matter in the haloes of some ellipticals are not that important. For example, Napolitano et al. (2005) have analysed the mass-to-light gradients of a sample of E + SO galaxies, and found that these are positive and important in massive, boxy E galaxies, but no very important for faint, disk E galaxies. This result is similar to that Romanowsky et al. (2003; see also Romanowsky 2006) have propound from the study of random velocities at the outskirts of E galaxies through PN, found to be low, and first interpreted by these authors as proving a dearth of dark matter in E galaxies, while Dekel et al. (2005) explain these large-radii low velocity dispersions as an effect of anisotropy and triaxiality of the halo stellar populations of these galaxies.

Assuming that ellipticals are embedded in massive haloes of dark matter, a second important concern is the possibility that their profiles have universal shapes. Here most inputs come from numerical simulations because observational inputs are scarce. When no dissipative processes are taken into account, spherically averaged dark matter density profiles of relaxed halos produced in N-body simulations have been found to be well fitted by analytical expressions such that, once rescaled, give essentially a unique mass density profile, determined by two parameters. These two parameters are usually taken to be the total mass, M_{vir} , and the concentration, c or the energy content, E . These two parameters are, on their turn, correlated (i.e., the mass-concentration relation, see, for example, Bullock et al. 2001; Wechsler et al. 2002; Manrique et al. 2003). When hydrodynamical forces and cooling processes enter the assembly of these halos and the baryonic objects they host, the dark matter profiles could be modified in the regions where baryons are dynamically dominant, due the so-called adiabatic contraction (see, for example, Blumenthal et al. 1986; Dalcanton, Spergel, & Summers 1997; Tissera & Domínguez-Tenreiro 1998; Gnedin et al. 2004). So, the shapes of dark matter haloes in ellipticals could deviate from the universal behaviour dark matter haloes produced in purely N-body simulations seem to follow.

Another important issue concerns the three dimensional cold baryon mass (i.e., stellar mass) distribution, and, more particularly, its distribution relative to the dark matter haloes: are ellipticals homologous systems or is the homology broken in their stellar mass distribution or in their *relative* dark- versus bright-mass distribution?

Concerning the three dimensional velocity distributions of the different elliptical components, very few is known either. In particular, the anisotropy of the stellar three-dimensional velocity dispersion tensor is hard to be observationally characterised. This is an important issue, however, not only because anisotropy plays an important role in the analyses of the elliptical dark matter content at several effective radii, but also because it could keep fossil informations about the physical processes involved in mass assembly and stellar formation in Es. The relative behaviour of the three-dimensional velocity dispersion tensors for the stellar and the dark mass components (i.e., the so-called kinematical segregation) is still more uncertain. There is not an unambiguous observational input about its presence in ellipticals, or about its possible systematic dependence with the elliptical mass scale. This is an important point because of its possible connection with the physical origin of the so-called Fundamental Plane (FP) relation, as different authors have suggested (Graham & Colless 1997; Busarello et al. 1997; Pahre, de Carvalho & Djorgovski 1998).

Understanding the FP relation (Djorgovski & Davis 1987; Dressler et al. 1987; Faber et al. 1987; Bernardi et al. 2003 and references therein) is in fact a milestone in the physics of elliptical formation. The FP is defined by the three observational parameters characterising

the mass and velocity distributions of their stellar component: luminosity L , radius at half projected light R_e^{light} , and central line-of-sight velocity dispersion $\sigma_{\text{los},0}$. The FP is tilted relative to the virial plane. Different authors interpret this tilt as caused by different misassumptions relative to the constancy of the dynamical mass-to-light ratios, M_{vir}/L , or the mass structure coefficients, $c_M^{\text{vir}} = \frac{GM_{\text{vir}}}{3\sigma_{\text{los},0}^2 R_e^{\text{light}}}$, with the mass scale (see discussion in Oñorbe et al. 2005, 2006, and references cited therein). Recently, these last authors have found that the samples of elliptical-like objects identified at $z = 0$ in their fully-consistent cosmological hydrodynamical simulations show systematic trends with the mass scale in both, the relative global dark-to-bright mass content, as well as in the relative sizes of the stellar and the dark mass components, giving rise to *dynamical* FPs.

We see that the mass or velocity distributions of the different E mass components encode a lot of informations about the physical origin of the FP, and, consequently, on the physics of E formation. We see also that, unfortunately, observational methods, by themselves, suffer from some drawbacks to deepen into these issues. A major drawback is that the informations on the intrinsical mass distribution are not directly available: we see the projections of luminosity (not three-dimensional mass) distributions. Another major drawback is that the intrinsic 3D velocity distribution of galaxies is severely limited by projection, only the line-of-sight velocity distributions can be inferred from galaxy spectra. And, so, the interpretation of observational data is not always straightforward. To complement the informations provided by data and circumvent these drawbacks, analytical modelling is largely used in literature (Kronawitter et al. 2000; Gerhard et al. 2001; Romanowsky & Kochanek 2001; Borriello, Salucci & Danese 2003; Padmanabhan et al. 2004; Mamon & Lockas 2005a, 2005b). They give very interesting insights into mass and velocity distributions, as well as the physical processes causing them, but are somewhat limited by symmetry considerations and other necessary simplifying hypotheses. These difficulties and limitations could be circumvented should we have at our disposal complete informations on the phase-space of the galaxy constituents. This is not possible through observations, but can be attained, at least in a virtual sense, through numerical simulations.

The first authors who studied the formation and properties of elliptical galaxies by means of numerical methods used purely gravitatory pre-prepared simulations. The origin of the FP was addressed, among others, by Capelato, de Carvalho & Carlberg (1995); González-García & van Albada (2003); Dantas et al. (2003); Nipoti, Londrillo & Ciotti (2003) and Boylan-Kolchin, Ma & Quataert (2005). Some of these authors (Dantas et al. 2003, Nipoti et al. 2003) conclude that dissipation must be a basic ingredient in elliptical formation. Bekki (1998) first considered the role of dissipation in elliptical formation through pre-prepared simulations. He adopts the merger hypothesis (i.e., ellipticals form by the mergers of two equal-mass gas-rich spirals) and he focuses on the role of the timescale for star formation in determining the structural and kinematical properties of the merger remnants. He concludes that the slope of the FP reflects the difference in the amount of dissipation the merger end products have experienced according with their luminosity (or mass). Recently, Robertson et al. (2006) have confirmed this conclusion on the role of dissipative dynamics to shape the FP, again through pre-prepared mergers of disk galaxies.

Apart from the FP relation origin, other aspects of the formation and evolution of elliptical galaxies have been analysed through pre-prepared simulations. For example, the different isophotal shapes ellipticals show and their kinematical support (either intrinsic rotation or anisotropic dispersion) has been addressed by A. Burkert and coworkers, who analysed in detail binary mergers of virtual galaxies with different morphologies and initial conditions (Naab & Burkert 2003; Naab & Trujillo 2006; Naab, Khochfar & Burkert 2006). Other-

wise, González-García, Balcells & Olshevsky (2006) analysed the velocity distribution of dissipationless binary merger remnants involving galaxies with different morphologies.

We see that pre-prepared simulations of merger events provide a very useful tool to work out the mass and velocity distributions of elliptical galaxies. They allow also to find out their links with the processes involved in galaxy assembly, but they are somewhat limited, for example by the fact that the probability of a particular initial setup at a given z is not known a priori, and that mergers involving more than two objects also occur and are frequent at high z s, so that some complementary informations must be provided, for example through semi-analytical models (Khochfar & Burkert 2005; Naab, Khochfar & Burkert 2006).

To overcome these limitations, a convenient method is to study the processes involved in galaxy formation in a *cosmological context* through *self-consistent* gravodynamical simulations. The method works as follows: initial conditions are set at high z , in an homogeneously sampled box, as a Montecarlo realization of the field of primordial fluctuations to a given cosmological model; then the evolution of these fluctuations is numerically followed up to $z = 0$ by means of a computer code that solves, in a periodic box, the gravitational and hydrodynamical evolution equations. This method allows us to follow the evolution of the dynamical and thermohydrodynamical properties of matter in the Universe; individual galaxy-like objects naturally appear as a consequence of this evolution. No prescriptions are needed as far as their mass assembly processes are concerned, only star formation processes need further modelling. The important point here is that self-consistent simulations *directly* provide with complete 6-dimensional phase-space informations on each constituent particle sampling a given galaxy-like object formed in the simulation, that is, they give directly the mass and velocity distributions of dark matter, gas and stars of each object.

Kobayashi (2005) has simulated the chemodynamical evolution of 74 fields with different cosmological cold dark matter initial spectra set in slowly rotating spheres, each of them with a 1.5 Mpc comoving radius and vacuum boundaries. So, these simulations are not yet fully self-consistent. She succeeded in reproducing the observed global scaling relations shown by elliptical galaxies, and, in particular, the FP relation, and the surface-brightness profiles, as well as the colour-magnitude and the mass-metallicity relations. She also analyses the role of major merger events and the timescales for star formation in shaping the mass and sizes of remnants.

Concerning self-consistent hydrodynamical simulations, Sommer-Larsen, Gotz & Portinari (2002) present first results on early-type galaxy formation in a cosmological context. Meza et al. (2003) present results of the dissipative formation of a compact elliptical galaxy in the Λ CDM scenario. Romeo, Portinari & Sommer-Larsen (2005) analyse the galaxy stellar populations formed in their simulations of galaxy clusters. Naab et al. (2005) got, from cosmological initial conditions, a spheroidal system whose photometric and kinematical properties agree with observations of ellipticals, in a scenario not including feedback from supernovae or AGN and not requiring recent major mergers. Interesting results on elliptical formation have also been obtained by de Lucia et al. (2005), from a semi-analytic model of galaxy formation grafted to the *Millennium Simulation*.

However, detailed analyses of the mass and velocity distributions of samples of virtual ellipticals formed in fully self-consistent hydrodynamical simulations, and, in particular, of the amount and distribution of dark matter relative to the bright matter distribution, as well as of the kinematics of the dark and bright components, and their successful comparison with observational data, were still missing. This is the work we present in this paper. To be specific, we have analysed the samples of virtual ellipticals formed in ten self-consistent hydrodynamical simulations, run in the framework of a flat Λ CDM cosmological model characterised by cosmological parameters consistent with their last determinations (Spergel

et al. 2006). Galaxy-like objects of different morphologies appear in these simulations at $z = 0$: disc-like objects, SO-like objects, elliptical-like objects (hereafter, ELOs) and peculiars.

Our previous work has shown that these ELO samples have properties that agree with observational data, so that they have counterparts in the real world. In fact, an analysis of the structural and dynamical ELO parameters that can be constrained from observations (i.e., stellar masses, projected half-mass radii, central line-of-sight velocity dispersions), has shown that they are consistent with those measured in the SDSS DR1 elliptical sample (Sáiz, Domínguez-Tenreiro & Serna 2004), including the FP relation (Oñorbe et al. 2005), and their lack of evolution at low and intermediate redshifts (Domínguez-Tenreiro et al. 2006, hereafter DTal06). Also, their stellar populations have age distributions showing similar trends as those inferred from observations, i.e., most stars have formed at high z on short timescales, and, moreover more massive objects have older means and narrower spreads in their stellar age distributions than less massive ones[†] (Domínguez-Tenreiro, Sáiz & Serna, 2004, hereafter DSS04).

The paper is organised as follows: in §2 we briefly describe the simulations and the star formation modelling. In §3, the ELO sample and the generic structure of ELOs are described. A brief account on ELO formation is given in §4. The three dimensional orbital structure of the baryonic component is briefly described in §5. §6 is devoted to report on the dark matter and baryonic mass density profiles of the ELOs produced in the simulations. In §7 we report on ELO circular velocity and velocity dispersion profiles. Finally, in §8 we summarise our results and discuss them in the context of theoretical results on halo structure and dissipation of the gaseous component and their connections with observational data.

2 THE SIMULATIONS

We have analysed ELOs identified in ten self-consistent cosmological simulations run in the framework of the same global flat Λ CDM cosmological model, with $h = 0.65$, $\Omega_m = 0.35$, $\Omega_b = 0.06$. The normalisation parameter has been taken slightly high, $\sigma_8 = 1.18$, as compared with the average fluctuations of 2dFGRS or SDSS galaxies (Spergel et al. 2006) to mimic an active region of the Universe (Evrard, Silk & Szalay 1990).

We have used a lagrangian code (DEVA, Serna, Domínguez-Tenreiro & Sáiz, 2003), particularly designed to study galaxy assembly in a cosmological context. Gravity is computed through an AP3M-like method, based on Couchman (1991). Hydrodynamics is computed through a SPH technique where special attention has been paid that the implementation of conservation laws (energy, entropy and angular momentum) is as accurate as possible (see Serna et al. 2003 for details, in particular for a discussion on the implications of violating some conservation laws). Entropy conservation is assured by taking into consideration the space variation of the smoothing length (i.e., the so-called ∇h terms). Time steps are individual for particles (to save CPU time, allowing a good time resolution), as well as masses. Time integration uses a PEC scheme. In any run, an homogeneously sampled periodic box of 10 Mpc side has been employed and 64^3 dark matter and 64^3 baryonic particles, with a mass of $m^{\text{dark}} = 1.29 \times 10^8$ and $m^{\text{b}} = 2.67 \times 10^7 M_\odot$, respectively, have been used. The gravitational softening used was $\epsilon = 2.3$ kpc. The cooling function is that from Tucker (1975) and Bond et al. (1984) for an optically thin primordial mixture of H and He ($X = 0.76$, $Y = 0.24$) in collisional equilibrium and in absence of any significant background radiation

[†] this is equivalent to the *downsizing* concept introduced by Cowie et al. (1996) to mean that star formation is stronger at low redshifts in smaller galaxies than in larger ones

field with a primordial gas composition. Each of the ten simulations started at a redshift $z_{\text{in}} = 20$.

Star formation (SF) processes have been included through a simple phenomenological parametrisation, as that first used by Katz (1992, see also Tissera, Lambas & Abadi 1997; and Serna et al. 2003 for details) that transforms cold locally-collapsing gas at the scales the code resolves, denser than a threshold density, ρ_{thres} , into stars at a rate $d\rho_{\text{star}}/dt = c_*\rho_{\text{gas}}/t_g$, where t_g is a characteristic time-scale chosen to be equal to the maximum of the local gas-dynamical time, $t_{\text{dyn}} = (4\pi G\rho_{\text{gas}})^{-1/2}$, and the local cooling time; c_* is the average star formation efficiency at resolution ϵ scales, i.e., the empirical Kennicutt-Schmidt law (Kennicutt 1998). It is worth noting that, in the context of the new sequential multi-scale SF scenarios (Vázquez-Semadeni 2004a and 2004b; Ballesteros-Paredes et al. 2006 and references therein), it has been argued that this law, and particularly so the low c_* values inferred from observations, can be explained as a result of SF processes acting on dense molecular cloud core scales when conveniently averaged on disc scales (Elmegreen 2002, Sarson et al. 2004, see below). Supernova feedback effects or energy inputs other than gravitational have not been *explicitly* included in these simulations. We note that the role of discrete stellar energy sources at the scales resolved in this work is not yet clear, as some authors argue that stellar energy releases drive gas density structuration locally at sub-kpc scales (Elmegreen 2002). In fact, recent MHD simulations of self-regulating SNII heating in the ISM at scales < 250 pc (Sarson et al. 2004), indicate that this process produces a Kennicutt-Schmidt-like law on average. If this were the case, the Kennicutt-Schmidt law implemented in our code would already *implicitly* account for the effects stellar self-regulation has on the scales our code resolves, and our ignorance on sub-kpc scale processes would be contained in the particular values of ρ_{thres} and c_* .

Five out of the ten simulations (the SF-A type simulations) share the SF parameters ($\rho_{\text{thres}} = 6 \times 10^{-25}$ gr cm $^{-3}$, $c_* = 0.3$) and differ in the seed used to build up the initial conditions. To test the role of SF parameterisation, the same initial conditions have been run with different SF parameters ($\rho_{\text{thres}} = 1.8 \times 10^{-24}$ gr cm $^{-3}$, $c_* = 0.1$) making SF more difficult, contributing another set of five simulations (hereafter, the SF-B type simulations).

3 SIMULATED ELLIPTICAL-LIKE OBJECTS AT $Z=0$: THE ELO SAMPLE

ELOs have been identified as those galaxy-like-objects having a prominent, relaxed spheroidal component, made out of stars, with no extended discs and very low cold gas content. Moreover, their dark-matter haloes must also be relaxed to allow their meaningful analysis, excluding systems that have just merged or that are about to merge. It turns out that, at $z = 0$, 26 (17) objects out of the more massive formed in SF-A (SF-B) type simulations fulfil these conditions. ELOs form two samples (the SF-A and SF-B ELO samples) partially analysed in Sáiz et al. (2004), in DSS04 and in DTal06. In Oñorbe et al. (2005, 2006) it is shown that both samples satisfy dynamical FP relations.

ELOs are embedded in dark matter haloes whose virial radii † are in the range $527 > r_{\text{vir}} > 191$ kpc. ELO stellar components have ellipsoidal shapes and have a lower limit in their stellar mass content of $3.8 \times 10^{10} M_{\odot}$ (see Kauffmann et al. 2003 for a similar result in SDSS galaxies). Inner discs, when present, are made out of cold gas. ELOs have also

† The virial radii, r_{vir} , have been calculated using the Bryan & Norman (1998) fitting formula, that yields, at $z = 0$, a value of $\Delta \simeq 100$ for the mean density within r_{vir} in units of the critical density

hot diffuse gas forming an extended halo (Sáiz, Domínguez-Tenreiro & Serna 2003). The number of dark and baryonic particles within r_{vir} are in the ranges $(5.3 \times 10^4, 2.4 \times 10^3)$ and $(3.1 \times 10^4, 2.0 \times 10^3)$, respectively, giving a lower limit in the virial masses of ELOs of $M_{\text{vir}} > 3.7 \times 10^{11} M_{\odot}$. Some ELOs show a clear net rotation, resulting in an average value of their spin parameter of $\bar{\lambda} = 0.033$. ELO mass function is consistent with that of a small group, that is a dense, environment (Cuesta-Bolao & Serna, private communication). ELOs in the SF-B sample tend to be of later type than their corresponding SF-A counterparts because forming stars becomes more difficult; this is why many of the SFB sample counterparts of the less massive ELOs in SFA sample do not satisfy the selection criteria, and the SFB sample has a lower number of ELOs than the SFA sample.

4 A BRIEF ACCOUNT ON ELO FORMATION

The simulations unveil the physical patterns of ELO mass assembly, energy dissipation and star formation (SF) rate histories (see Sierra Glez. de Buitrago et al. 2003; DSS04, DTal06). Our simulations indicate that ELOs are assembled out of the mass elements that at high z are enclosed by those overdense regions R whose local coalescence length $L_c(t, R)$ (Vergassola et al. 1994) grows much faster than average, and whose mass scale (total mass enclosed by R , M_R) is of the order of an E galaxy virial mass. Analytical models, as well as N-body simulations indicate that two different phases operate along halo mass assembly: first, a violent fast one, where the mass aggregation rates are high, and then, a slower one, with lower mass aggregation rates (Wechsler et al. 2002; Zhao et al. 2003; Salvador-Solé, Manrique, & Solanes 2005). Our hydrodynamical simulations indicate that the fast phase occurs through a multiclump collapse (see Thomas, Greggio & Bender 1999) ensuing turnaround of the overdense regions, and it is characterised by the fast head-on (that is, with very low relative orbital angular momentum) fusions experienced by the nodes of the cellular structure these regions enclose, resulting in strong shocks and high cooling rates of their gaseous component, and, at the same time, in strong and very fast star SF bursts that transform most of the available cold gas in R into stars. For the massive ELOs in this work, this happens between $z \sim 6$ and ~ 2.5 and mainly corresponds to a cold mode of gas aggregation, as in Keres et al. (2005). Consequently, most of the dissipation involved in the mass assembly of a given ELO occurs in this violent early phase at high z ; moreover, its rate history [§] is reflected by the star SF rate history, as illustrated in figure 1 of DTal06. The Fundamental Plane relation shown by elliptical galaxies appears in this fast violent phase as a consequence of dissipation and homology breaking in the mass distribution (see Oñorbe et al. 2005, 2006 and DTal06).

The slow phase comes after the fast phase. In this phase, the halo mass aggregation rate is low and the M_{vir} increment results from major mergers, minor mergers or continuous mass accretion. Our cosmological simulations show that the fusion rates are generally low and that these mergers generally imply only a modest amount of energy dissipation or star formation. In fact, a strong SF burst and dissipation follow a major merger only if enough gas is still available after the early violent phase. This is unlikely in any case, and it becomes more and more unlikely as M_{vir} increases (see DSS04). A consequence of the lack of dissipation is that the Fundamental Plane is roughly preserved along the slow phase (see DTal06). We have to point out that mergers play an important role in this slow phase as far as mass assembly is concerned: an $\sim 50\%$ of ELOs in the sample have experienced a major merger event at

[§] That is, the amount of cooling per time unit experienced by those gas particles that at $z = 0$ form the ELO stellar component

$2 < z < 0$, that result in the increase of the ELO mass content, size and stellar mean square velocity. Some of these mergers are multiple, and in some few cases, either binary or multiple mergers involve disk galaxies, but none of the ELOs in our sample has been shaped by a merger of two or more adult disk virtual galaxies, maybe because our simulated box mimics a dense environment.

So, our simulations suggest that most of the stars of to-day ellipticals, or at least of those in dense environments, could have formed at high redshifts, while they are assembled later on (see de Lucia et al. 2005, for similar results from a semi-analytic model of galaxy formation grafted to the *Millennium Simulation*). This formation scenario shares some aspects of both, the hierarchical merging and the monolithic collapse scenarios, but it has also significant differences, mainly that most stars belonging to Es form out of cold gas that had never been shock heated at the halo virial temperature and then formed a disk, as the conventional recipe for galaxy formation propounds (see discussion in Keres et al. 2005 and references therein). An important point is that our simulations indicate that this formation scenario follows from simple physical principles in the context of the current Λ CDM scenario.

5 THREE DIMENSIONAL STRUCTURE OF THE BARYONIC CONSTITUENT

A quantitative description of ELO mass distributions is given by their 3D density profile and the structure their constituent particles. We first address the structure of the baryonic particles.

5.1 Three dimensional structure for gas particles

The gas structure is drawn in Figure 1 for the second more massive object formed in a SF-B type simulation. The 3D density at a given distance, r , from the centre of the object has been calculated by binning on concentric spherical shells around r . In this Figure, the line is the density profile of dark matter around the object, multiplied by Ω_b/Ω_m . Points represent gas density at the positions of SPH particles, and colours stand for gas particle temperatures according with the scale at the bottom of the Figure.

We see in this Figure that very few gas is left at positions with $r \leq 30$ kpc where stars dominate the mass density, that cold gas at $r \geq 30$ kpc is dense and clumpy, while hot gas (that is, gaseous particles with $T > 3 \times 10^4$ K) is diffuse with an almost isothermal component at $100 \text{ kpc} \leq r \leq 400 \text{ kpc}$, and a warm component at the outskirts of the configuration, reaching outside the virial radius (395.0 kpc). Two scales stand out in this configuration: the *ELO scale* or stellar component, with a size in this case of ~ 30 kpc, and the *halo scale*, a halo of dark matter of 395.0 kpc. Cold dense gas particles are associated in most cases with small dark matter haloes (not seen in the Figure); both gaseous particles in cold clumps and dark matter particles in their (sub)haloes are *shocked* particles, using the terminology of the adhesion model (see, for example, Vergassola et al. 1994). The configuration illustrated by this Figure is generic for ELOs: we can distinguish an *ELO scale*, with typical sizes of no more than $\sim 10 - 40$ kpc, and the *halo scale*, a halo of dark matter typically ten times larger in size.

5.2 Stellar and gaseous particle orbits

ELO constituent particles of different kinds travel on orbits that have different characteristics. To analyse this point, in the upper panel of Figure 2 we plot, for each star particle

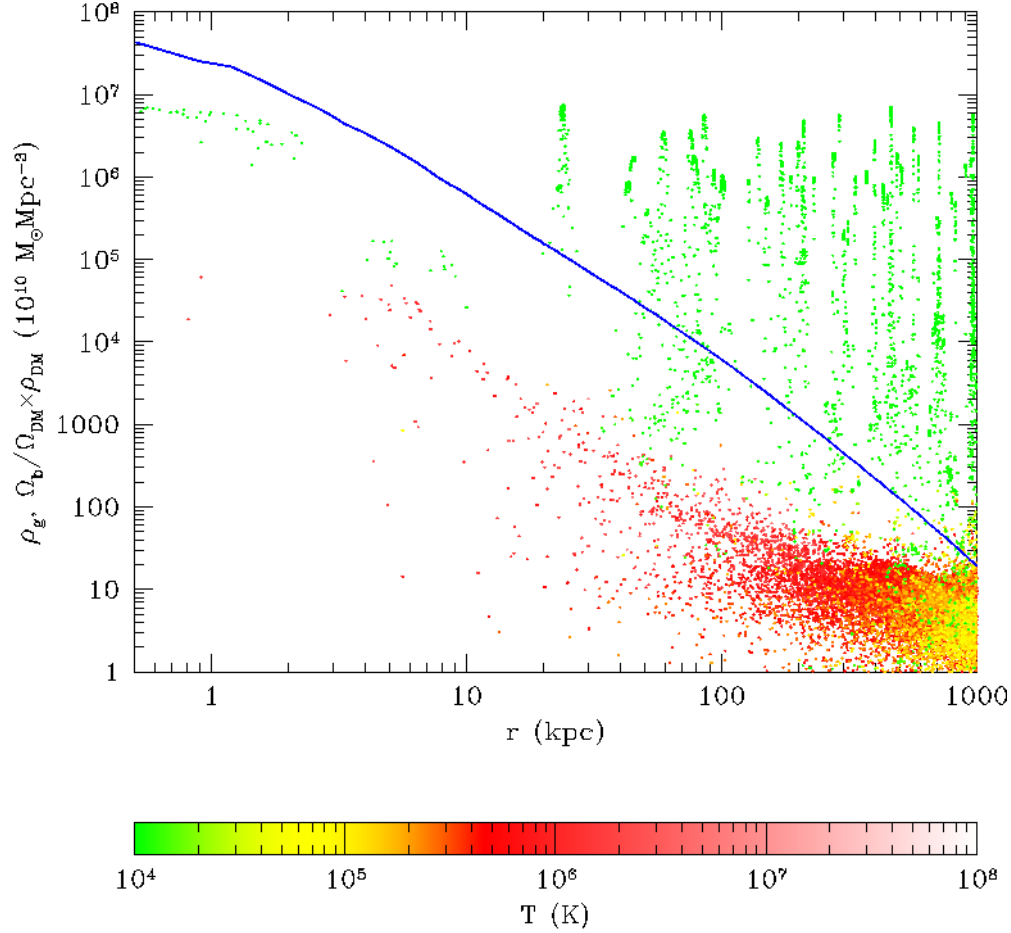


Figure 1. 3D gas (points) and dark matter (blue line) density for a typical ELO. Note the dense cold gas clumps embedded in the diffuse hot gas component. See text for an explanation.

and each gaseous particle of a typical ELO, the cosine of the angle formed by its position (\vec{r}_i) and its velocity (\vec{v}_i) as a function of r_i . Positions and velocities have been taken with respect to the centre of mass of the main baryonic object. In this plot radial orbits have cosines = ± 1 , while circular orbits have cosines = 0. Starred (circular) symbols stand for stellar (gaseous) particles. We see that cold gas particles at $r \leq 4$ kpc form a disc in coherent circular motion; filled (open) symbols represent particles in corotation (counterrotation) with respect to this small disc. We can also see that stellar particle orbits at ≤ 3 kpc scales do not show any preference, while those further away, as well as gaseous particles outside the disc, show a slight tendency to be on radial orbits providing anisotropy to the velocity dispersion. Stellar particles constitute a disordered or dynamically hot component, showing an important velocity dispersion, and, also, in some cases, a coherent net rotation. In §7 these issues will be addressed in detail.

6 THE DARK MATTER AND BARYONIC MASS DISTRIBUTIONS

6.1 Dark matter profiles

Spherically averaged dark matter density profiles of relaxed halos formed in N-body simulations have been found to be well fitted by analytical expressions such that, once rescaled, give essentially a unique mass density profile i.e., a two parameter family. These two param-

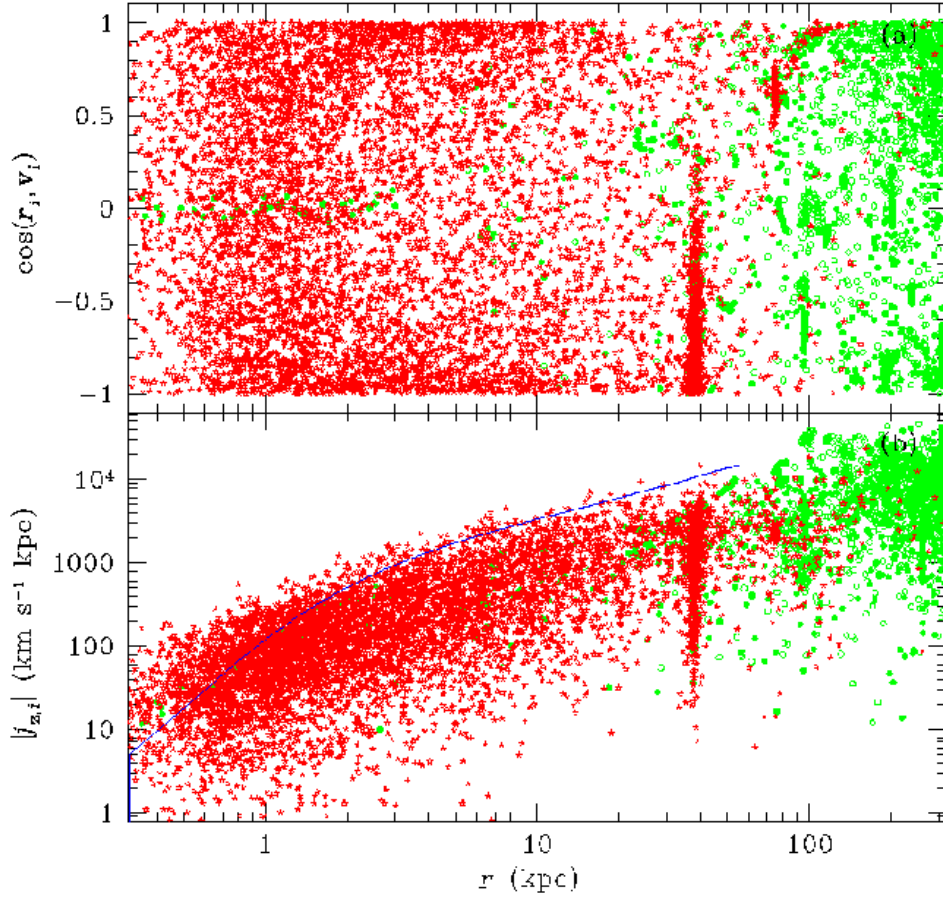


Figure 2. Upper panel: the cosine of the angle formed by the position and the velocity vectors for each gaseous (green circles) and stellar (starred red symbols) particle belonging to a typical ELO. Filled (open) symbols stand for particles in (counter) corotation with the small inner disc

eters are usually taken to be the total mass, M_{vir} , and the concentration, c or the energy content, E . These two parameters are, on their turn, correlated (i.e., the mass-concentration relation, see, for example, Bullock et al. 2001; Wechsler et al. 2002; Manrique et al. 2003) because the assembly process implies a given correlation between M_{vir} and E . Different authors propound slightly different fitting formulae, see Hernquist 1990 (Hern90), Navarro, Frenk & White 1995, 1996 (NFW), Tissera & Domínguez-Tenreiro 1998 (TD), Moore et al. 1999 (M), Jing & Suto 2000 (JS) and Navarro et al. 2004 (Nav04), that can be written as:

$$\rho_{\text{h}}^{\text{dark}}(r) = 3c^3 \rho_{\Delta}^{\text{aver}} g(c) \times \rho(r/a_h) \quad (2)$$

where $\rho_{\Delta}^{\text{aver}}$ is the average density within the virial radii, $c \equiv r_{\text{vir}}/a_h$ is the so-called concentration parameter, and

$$\rho(y) = y^{-\alpha} (1 + y)^{-\beta}, \quad (3)$$

where $(\alpha, \beta) = (1, 3)$ for Hern90; $(\alpha, \beta) = (1, 2)$ for NFW; $(\alpha, \beta) = (2, 2)$ for TD, and $\beta = 3 - \alpha$, with α left free, for the general formula found by Jing & Suto (2000) (note that NFW can be considered as JS with $\alpha = 1$). In these fitting formulae α is the inner slope ($r \ll a_h$), the outer slope ($r \gg a_h$) is $\alpha + \beta$ (3 for JS or NFW), so that a_h characterises the scale where the slope changes. Other interesting scale is r_{-2} , the r value where the

logarithmic slope, $d \ln \rho / d \ln r = -2$. We have $r_{-2} = a_h(2 - \alpha)/(\alpha + \beta - 2)$ for a profile given by Eq. 3, with $r_{-2} = a_h(2 - \alpha)$ for JS and $r_{-2} = a_h$ for NFW. Navarro et al. (2004) propound a different fitting formula of the form:

$$\rho(y) = \exp(-2\mu y^{1/\mu}). \quad (4)$$

where $d \ln \rho / d \ln r = -2(r/a_h)^{1/\mu}$ and $r_{-2} = a_h$.

The $g(c)$ functions can be written as:

$$g(y) = y^2/2(y+1)^2 \text{ (Hern90)} \quad (5)$$

$$g(y) = \ln(y+1) - y/(y+1) \text{ (NFW)} \quad (6)$$

$$g(y) = 9y/(1+y) \text{ (TD)} \quad (7)$$

$$g(y) = (3-\alpha)^{-1} y^{3-\alpha} {}_2F_1(3-\alpha, 3-\alpha, 4-\alpha, -y) \text{ (JS)} \quad (8)$$

$$g(y) = \rho_{-2} \exp(2\mu)/(3c^3 \rho_\Delta) \text{ (Nav04)} \quad (9)$$

where ρ_{-2} is the average density within r_{-2} and ${}_2F_1$ is the hypergeometric function.

When processes other than gravitational are involved in mass assembly (for example, cooling or heating), the dark matter density profiles could be modified (see Blumenthal et al. 1986; Dalcanton et al. 1997; Tissera & Domínguez-Tenreiro 1998; Gnedin et al. 2004). To analyse this point, in Figure 3 we plot the dark matter density profiles for several typical ELOs, along with their best fit to different analytical profiles. The optimal fit has been obtained by minimising the statistics:

$$\chi^2 = \sum_{i=1}^N [\log M(< r_i) - \log M_{\text{ELO}}^{\text{dark}}(< r_i)]^2 / N \quad (10)$$

where $M_{\text{ELO}}^{\text{dark}}(< r_i)$ is the ELO dark matter mass within a sphere of radius r_i centred at its centre of mass, $M(< r_i)$ is the integrated mass density profile corresponding to the different formulae above, and the virial radii r_{vir} have been taken as outer boundaries of the fitting range. The *integrated* dark matter density profiles have been used as fitting formulae instead of the dark matter density profiles themselves because these latter are binning dependent. An updated version of the MINUIT software from the CERN library has been used to make these fits as well as the others in this paper.

Note in Figure 3 that the quality of the fits differs from one analytical profile to another. To quantify this effect, in Figure 4 we plot the distributions of the χ^2 per d.o.f. statistics, normalised to $(\log M_{\text{vir}})^2$, resulting from the fits to the different profiles above, except for Hern90 one whose results are generally poorer. We see that the lower χ^2 per d.o.f. values generally correspond to either the Nav04 or the JS profiles, with the TD profiles in the third position. In Figure 5 we draw the values of the μ (for Nav04 profiles) and α (for JS profiles) slopes corresponding to the optimal fits of SF-A sample DM haloes. A slight mass effect can be appreciated with lower mass ELOs having steeper DM haloes than more massive ones, presumably due to a more important pulling in of baryons onto dark matter as they fall to the ELO centre with decreasing ELO mass. That is, massive haloes are less concentrated than lighter ones, i.e., the mass-concentration relation. In any case, the profiles are always steeper than $\alpha = 1$ (i.e., the NFW profile; see Mamon & Lockas 2005a).

To further analyse this effect, in Figure 6 we plot the ρ_{-2} density parameter versus the r_{-2} scale obtained from fits to the Nav04 formula. Blue triangles are measurements by Navarro et al. (2004) onto haloes formed in N-body simulations and the green line is their best fit. We see that at given r_{-2} , ρ_{-2} is higher in our hydrodynamical simulations than in Nav04, presumably due to the pulling in of dark matter by baryon infall. We also see that at given M_{vir} , r_{-2} is shorter in hydrodynamical simulations than in purely gravitatory ones, by the same reason.

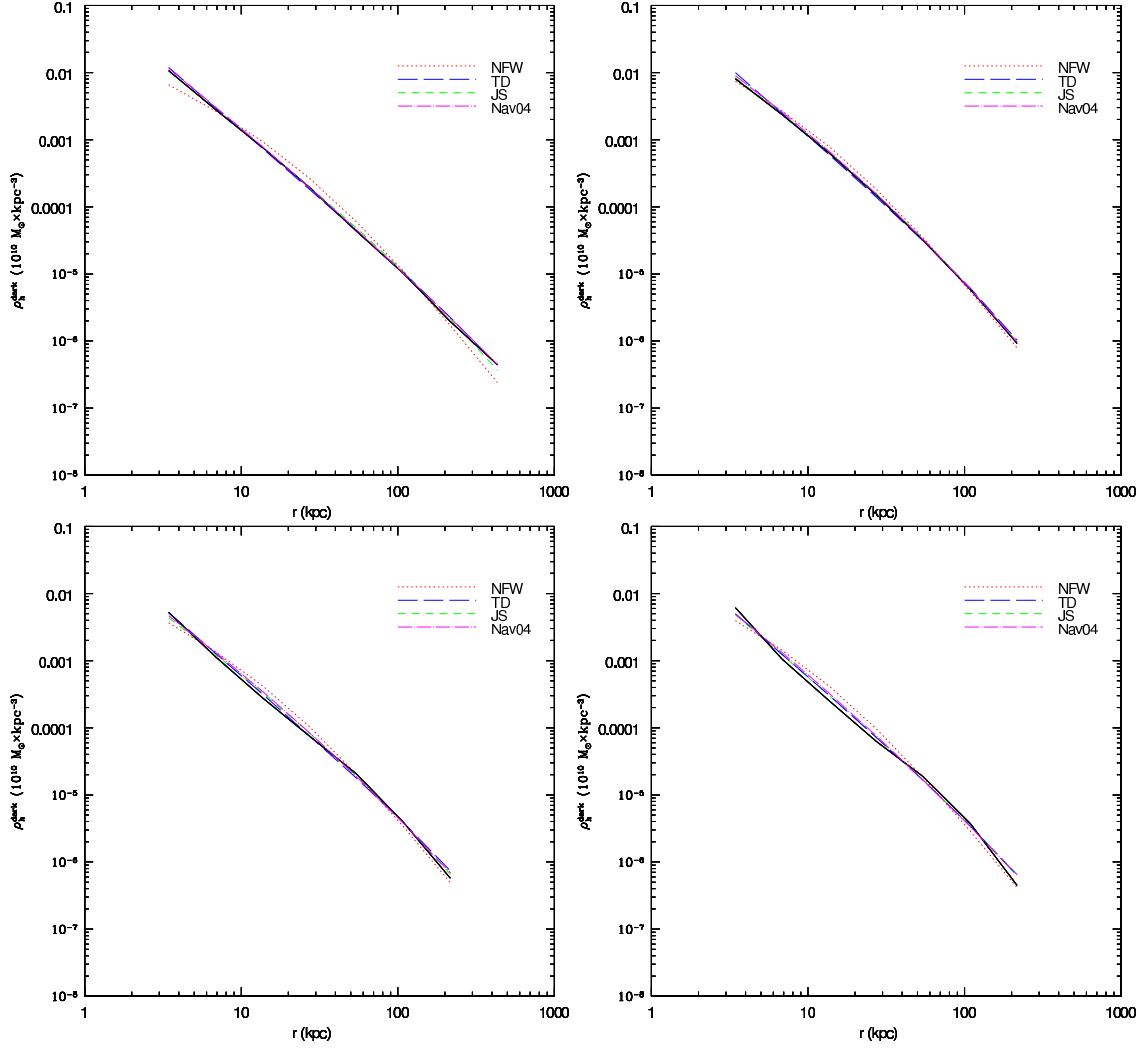


Figure 3. Dark matter density profiles (black full line) for several typical ELOs from SF-A and SF-B samples along with their best fits to different analytical profiles: NFW (red point line), TD (blue long-dashed line), JS (green short-dashed line) and Nav04 (magenta point-dashed line).

6.2 Projected stellar mass density profiles

Authors now agree that the Sérsic law given in Eq. 1 (Sérsic 1968) is an adequate empirical representation of the optical surface brightness profiles of most ellipticals (see, for example, Caon et al. 1993; Bertin et al. 2002). Assuming that the stellar mass-to-light ratio γ^{star} does not appreciably change with ELO projected radius R [¶], the projected stellar *mass* profile, $\Sigma^{\text{star}}(R)$ can be taken as a measure of the surface *brightness* profile and be written as

$$\Sigma^{\text{star}}(R) = \gamma^{\text{star}} I^{\text{light}}(R). \quad (11)$$

One can then expect that $\Sigma^{\text{star}}(R)$ can be fitted by a Sérsic-like law. This is in fact the case as shown in Figure 7 for several typical ELOs drawn from both SF-A and SF-B samples. Some remarks on how the fits have been made are in order. First, the $\Sigma^{\text{star}}(R)$ profiles have been calculated by averaging on concentric rings centred at the projection of the centre-of-mass of the corresponding ELO. Three projections along orthogonal directions have been

[¶] Hereafter we will use capital R to mean projected radii

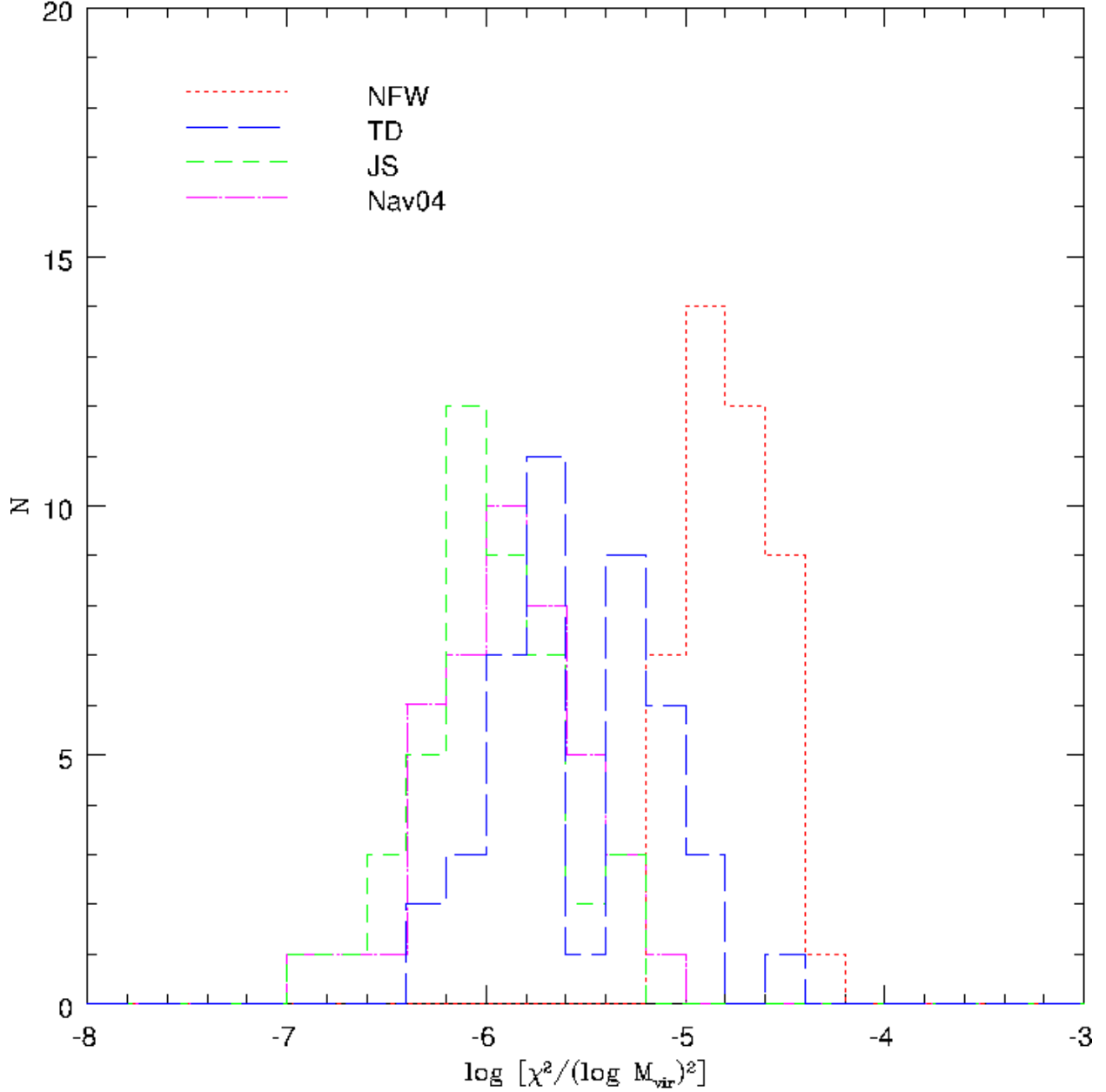


Figure 4. The distributions of the χ^2 per d.o.f., normalised to the logarithm of their respective mass square, for the fits of the DM density profiles of ELO haloes (SF-A and SF-B samples) to different analytical profiles

considered for each ELO. Also, because these projected densities are binning dependent and somewhat noisy, the integrated projected mass density in concentric cylinders of radius R and mass

$$M_{\text{cyl}}^{\text{star}}(R) = 2\pi \int_0^R \Sigma^{\text{star}}(R') R' dR' \quad (12)$$

has been used as a fitting function, instead of $\Sigma^{\text{star}}(R)$ itself. Concerning the fitting range, we have adopted an outer boundary R_{max} such that the corresponding surface brightness $I^{\text{light}}(R_{\text{max}})$ (see Eq. 11) gives the standard value of $\mu_B = 27 \text{ mag arcsec}^{-2}$. The values for the stellar mass-to-blue-light γ_B^{star} span a range from $\gamma_B^{\text{star}} = 2$ to 12, depending on the details of its determination (see discussion in Mamon & Lockas 2005a), and best values of $\gamma_B^{\text{star}} = 5$

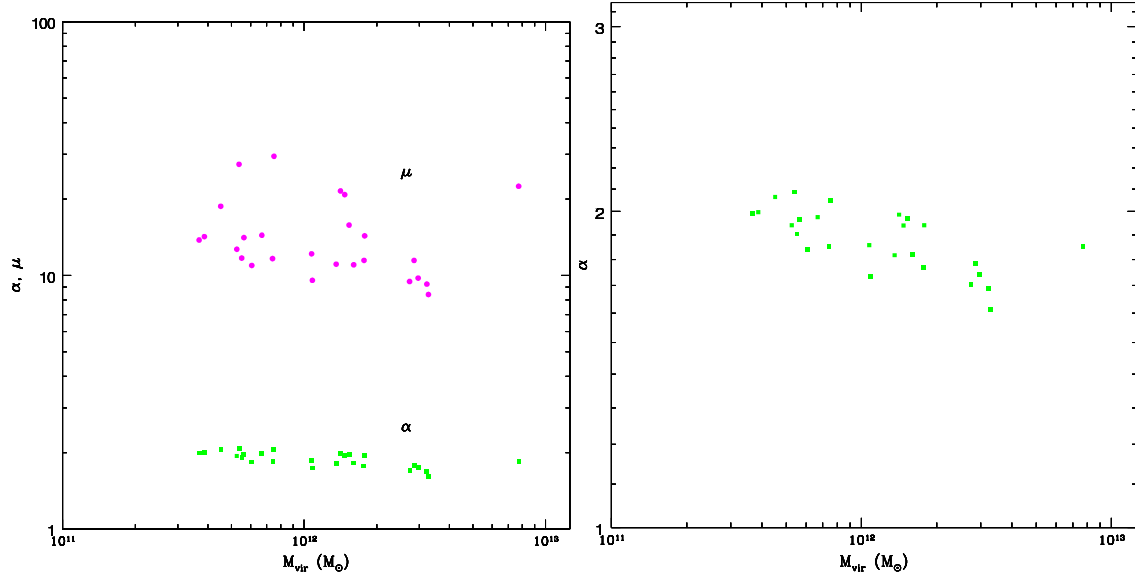


Figure 5. Left panel: the optimal inner slope α of the general Jing & Suto profile for the DM haloes of ELOs (green filled squares) and the μ coefficient of the Nav04 analytical profile (magenta filled circles), versus their virial mass for SF-A sample ELOs. Right panel: zoom of the α versus virial mass plot to clarify the mass effect.

to 8. Their geometric mean $\gamma_B^{\text{star}} = 6.3$ has been used to make the fits drawn in Figure 7, but the results of the fit do not significantly depend on the particular γ_B^{star} value used within its range of best values.

An interesting result is that the values of the shape parameter n we have obtained are consistent with observations, including their correlations with the effective radii R_e^{light} , luminosity L and velocity dispersion (Caon et al. 1993; Prugniel & Simien 1997; Graham 1998; Márquez et al. 2000; D’Onofrio 2001; Trujillo et al. 2001; Vazdekis, Trujillo & Yamada 2004), as illustrated in Figure 8. In this Figure we plot the shape parameter n versus the ELO projected stellar half-mass radii, $R_{e,\text{bo}}^{\text{star}}$, defined by the condition that $M_{\text{cyl}}^{\text{star}}(R_{e,\text{bo}}^{\text{star}})$ encloses half the total stellar mass of the system; assuming that γ_B^{star} does not depend on R , we will have $R_{e,\text{bo}}^{\text{star}} \simeq R_e^{\text{light}}$. Blue triangles are data on n and R_e^{light} from D’Onofrio (2001). Note that a slight effect resulting from the different SF parametrisation in SF-A and SF-B sample ELOs is apparent in this plot, mainly due to the smaller sizes of SFB sample ELOs as compared with their SFA sample counterparts.

6.3 Baryonic three-dimensional mass density profiles

In the last section it has been shown that the projected stellar mass density profiles are adequately described by the standard Sérsic profiles, that is, that they are consistent with observational data. We now analyse the three-dimensional mass density profiles of baryons.

We first analyse the baryon distribution at the ELO scale, where the main contribution to the mass density comes from stars. We lack of any observational input on how the three-dimensional stellar-mass density profiles $\rho^{\text{star}}(r)$ can be, except for a deprojection of the Sérsic profiles (Prugniel & Simien 1997; Lima Neto, Gerbal & Márquez 1999). In Figure 9 we plot $\rho^{\text{star}}(r)$ for ELOs in the SF-A sample. Different colours have been used for ELOs in different mass intervals and a clear mass effect can be appreciated in this Figure, and particularly so at the inner regions, where at fixed r/r_{vir} the stellar-mass density of less massive ELOs can be a factor of two or so higher than that of more massive ones. This means that the mass homology is broken in the three-dimensional stellar mass distribution.

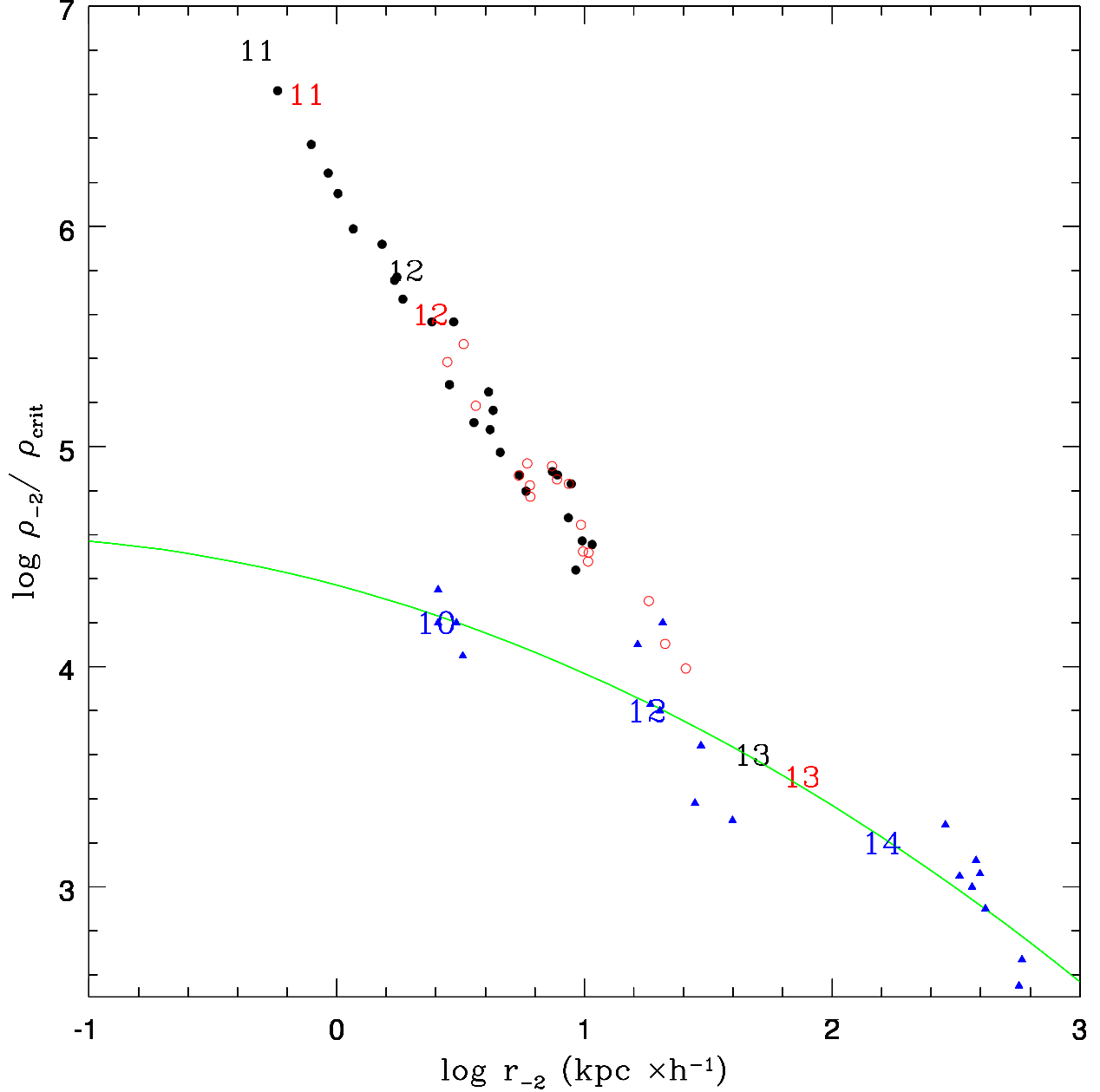


Figure 6. The ρ_{-2} density parameter versus the r_{-2} scale obtained from fits to the Nav04 formula, for ELOs in both the SF-A sample (filled black circles) and the SF-B sample (open red circles). Blue triangles are measurements by Navarro et al. 2004, onto haloes formed in N-body simulations, with its fit by Mamon & Lockas 2005a (green line). Numbers correspond to the logarithms of the virial masses (in units of M_{\odot}) of haloes formed in different simulations, according with their respective colours

To quantify the stellar three-dimensional mass density profiles of ELOs, they have been fit to JS and Nav04 analytical formulae through the statistics defined in Eq. 10 where $M_{\text{ELO}}^{\text{dark}}(< r_i)$ has been replaced by the ELO stellar mass within a sphere of radius r_i . The quality of the fits is illustrated in Figure 10, and in Figure 11 the values of the χ^2 p.d.o.f. statistics are given, normalised to $\log M_{\text{bo}}^{\text{star}}$. Both Figures show that these profiles describe adequately well the spherically-averaged stellar mass distribution in three dimensions, even if with very small r_{-2} values.

To study the possibility that the homology in the dark- versus bright-mass distribution is also broken, the stellar-to-dark density ratio profiles

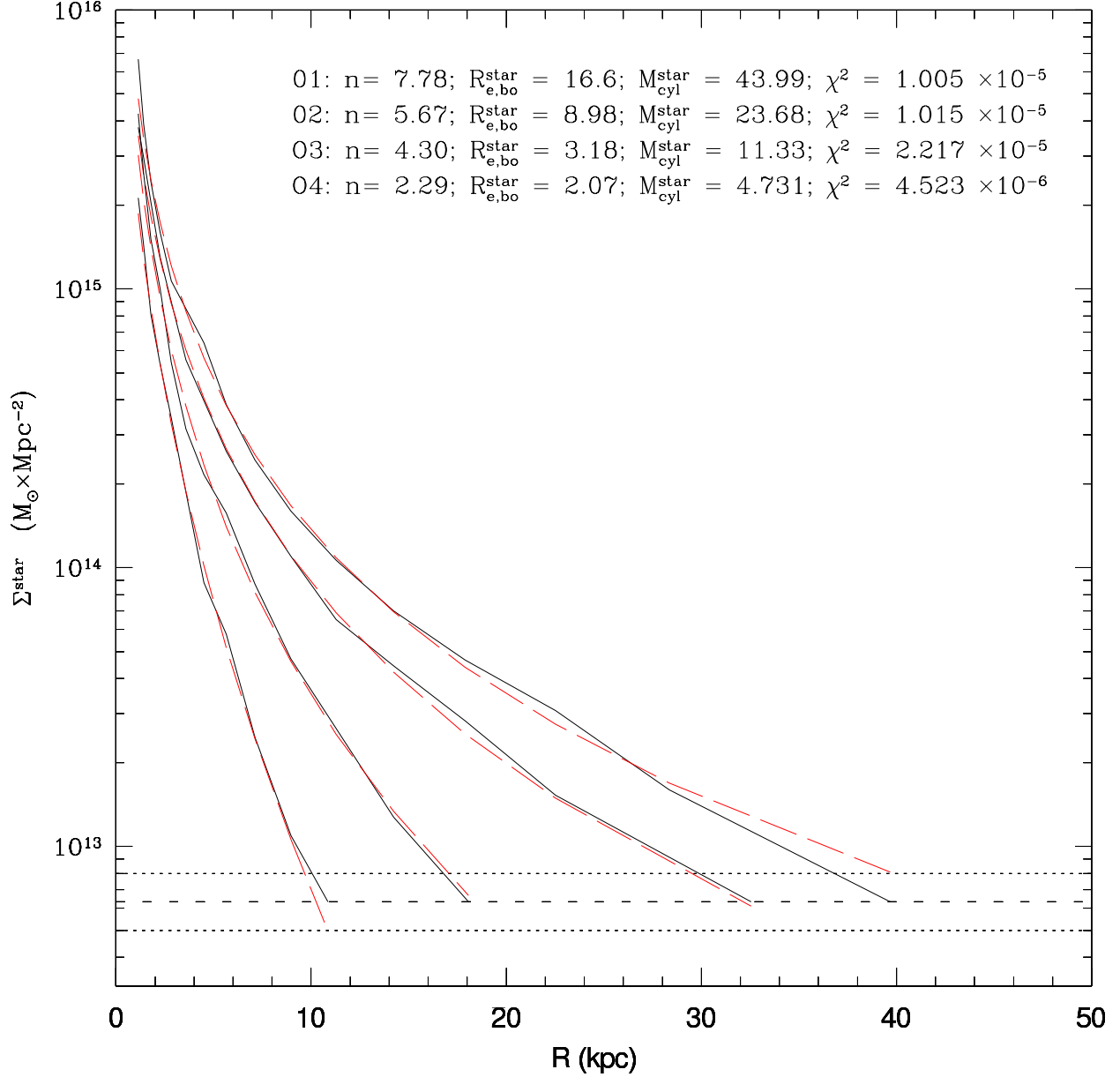


Figure 7. Projected stellar mass density profiles for different ELOs along with their best fit by a Sérsic law. The corresponding shape parameter best values and minimal χ^2 per-degree-of-freedom are also shown

$$f_{\rho}^{star}(r) = \rho^{star}(r) / \rho^{dark}(r) \quad (13)$$

are plot versus either the radii (Figure 12 upper panel) or the radii normalised to virial radii (Figure 12 lower panel). We see that there is, in any case, a clear mass effects at the inner regions, with the stellar mass distribution relative to the dark mass one less concentrated with increasing ELO mass. For example, in Figure 12 we see that the fraction of the ELO virial volume where $f_{\rho}^{star}(r) > 1$, is smaller as the ELO mass grows; also, at fixed r/r_{vir} , $f_{\rho}^{star}(r)$ increases with decreasing ELO mass. So, the homology is broken in the three-dimensional stellar-to-dark mass distribution, a fact that could be important to explain the tilt of the observed FP (see Oñorbe et al. 2005, 2006).

To further analyse this point and make the comparison with observational results easier, the dark-to-stellar mass ratio profiles, $M^{dark}(< r) / M^{tot}(< r)$, are drawn in Figure 13 for

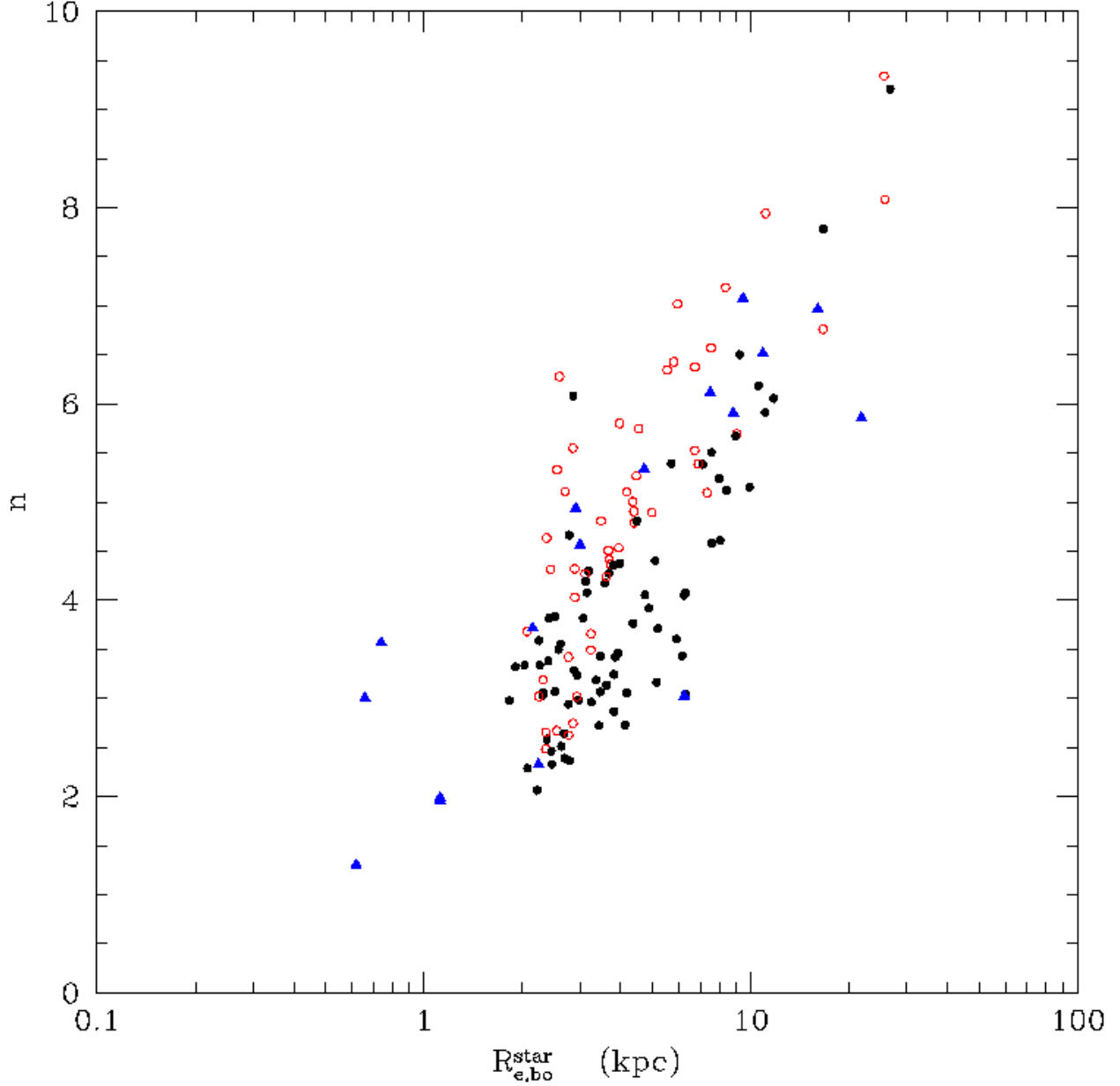


Figure 8. The Sérsic shape parameter n versus the projected stellar half-mass radii for SF-A sample (black filled circles) and SF-B sample (red open circles) ELOs. For each ELO, the results of projections along three orthogonal directions are shown. Blue filled triangles are data on n and R_e^{light} from D’Onofrio (2001)

the same ELOs, with the radii in units of the three dimensional stellar half-mass radii^{||}. We see that there is, in any case, a positive gradient, and again a clear mass effect, with a tendency of the dark matter fraction at fixed values of $r/r_{e,bo}^{\text{star}}$ to be higher as the mass scale increases. To be more quantitative and compare with observational data, we plot in Figure 14, upper panel, the fraction of dark-to-total masses at $r/R_{e,bo}^{\text{star}} = 1$ for ELOs in the SF-A and SF-B samples, versus their stellar masses. The differences among results for both samples come from the smaller $R_{e,bo}^{\text{star}}$ values of SFB sample ELOs as compared with

^{||} The effective or stellar half-mass radii $r_{e,bo}^{\text{star}}$ are defined as the radii of the spheres enclosing half the ELO stellar mass. This is the relevant three-dimensional size parameter at ELO scales. See Oñorbe et al. (2006) for details

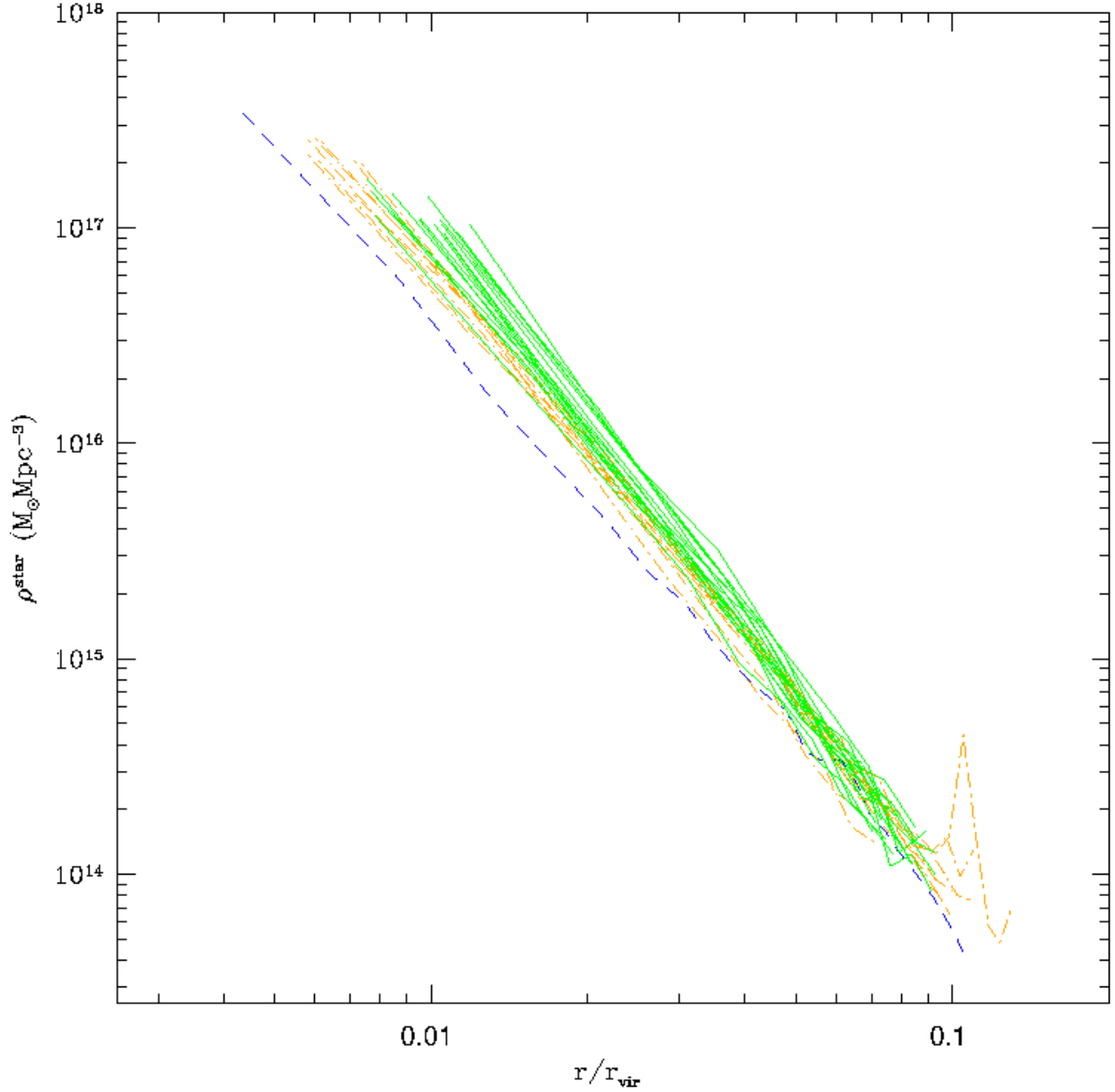


Figure 9. Three-dimensional stellar mass profiles for ELOs in the SF-A sample: full green lines, ELOs with $M_{\text{vir}} < 1.5 \times 10^{12} M_{\odot}$; orange point-dashed lines, ELOs with $1.5 \times 10^{12} M_{\odot} \leq M_{\text{vir}} < 5 \times 10^{12} M_{\odot}$; blue dashed lines: ELOs with $M_{\text{vir}} \geq 5 \times 10^{12} M_{\odot}$. The stellar mass density profiles show homology breaking

their SFA counterparts (see details in Oñorbe et al. 2006). Blue triangles with error bars are results from integral field SAURON data and models by Cappellari et al. 2006. We see that these empirical determinations of the dark matter fraction at the centre of ellipticals is consistent with the values found in ELOs of both samples, including its growth with the mass scale.

In the lower panel of Figure 14 we give the gradients of the $M^{\text{dark}}(< r)/M^{\text{star}}(< r)$ profiles as a function of their stellar masses. Blue triangles with error bars are the empirical mass-to-light gradients as determined by Napolitano et al. 2005 for elliptical galaxies with isophotal shape $a_4 \times 100 < 0.1$, that is, boxy ellipticals. We have used as inner and outer radii $r/r_{\text{e,bo}}^{\text{star,in}} = 0.5$ and $r/r_{\text{e,bo}}^{\text{star,out}} = 4$, roughly the average values of the inner and outer radii these authors give in their Table 1. We see that there is a mass effect and that our results are

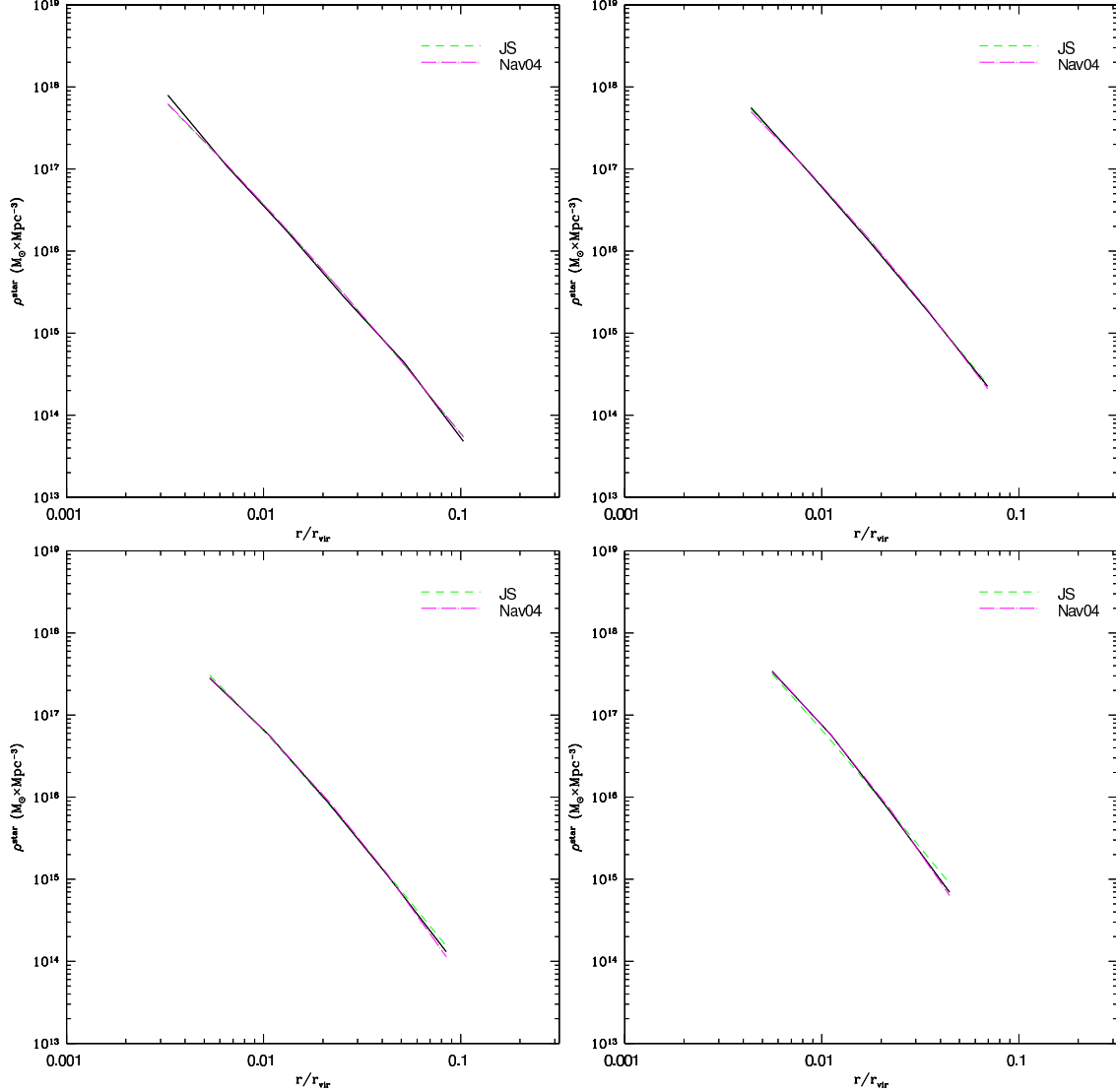


Figure 10. The stellar mass profiles for 4 typical ELOs in SF-A sample (black continuous lines) and their optimal fits to Nav04 profiles (magenta point-dashed lines) and JS profiles (green dashed lines)

consistent with those found by these authors in the range of stellar mass values our samples span, especially when we consider that ELOs in our samples are boxy (see §7.2). A SF effect in the stellar mass distribution also appears in Figure 14, again due to the compactness of the SFB sample ELOs relative to their SFA sample counterparts.

We now turn to analyse the baryon space distribution at halo scales. To have an insight on how baryons of any kind are distributed relative to the dark matter at the halo scale and beyond, the baryon fraction profile

$$f^{\text{ab}}(r) = \rho^{\text{ab}}(r) / \rho^{\text{tot}}(r), \quad (14)$$

where "ab" stands for baryons of any kind (i.e., stars, cold gas and hot gas) and "tot" stands for matter of any kind (i.e., dark plus baryons of any kind), is drawn in Figure 15 for ELOs in the SF-A sample (black full lines) and in the SF-B sample (red point lines) in the same range of virial mass, $1.5 \times 10^{12} M_{\odot} \leq M_{\text{vir}} < 5 \times 10^{12} M_{\odot}$. Despite individual characteristics, the $f^{\text{ab}}(r)$ curves show a typical pattern in which their values are high at the centre, then they decrease and have a minimum lower than the global value, $f_{\text{cosmo}}^{\text{ab}} \equiv$

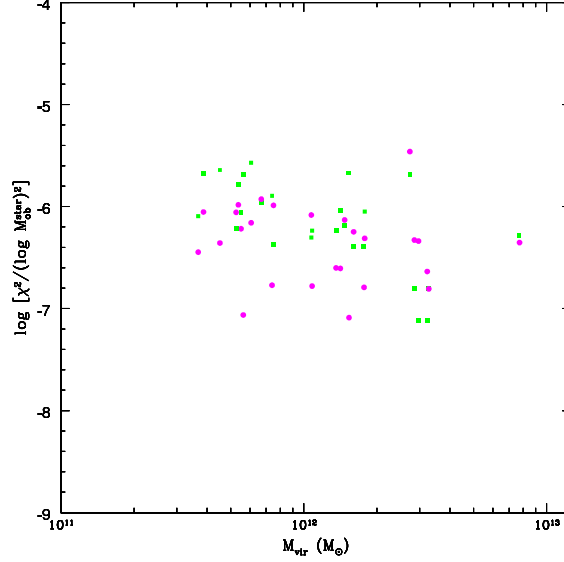


Figure 11. The χ^2 statistics (Eq. 10) corresponding to the fits of the stellar mass profiles for ELOs in the SFA-sample Nav04 profiles (magenta filled circles) and JS profiles (green filled squares)

$\Omega_b/\Omega_m = 0.171$, at a radius r_{\min}^{ab} , then they increase again, reach a maximum value and then they decrease and fall to the $f_{\text{cosmo}}^{\text{ab}}$ value at a rather large r value, larger than the corresponding virial radii. This result, i.e., that elliptical galaxies are not baryonically closed, is also indicated by recent X-ray observations (Humphrey et al. 2006). Notice (Figure 16) that the increase of $f^{\text{ab}}(r)$ at $r > r_{\min}^{\text{ab}}$ is mainly contributed by hot gas, almost absent at $r < r_{\min}^{\text{ab}}$, indicating that r_{\min}^{ab} separates the (inner) region where gas cooling has been possible from the (outer) region where gas has not had time enough to cool in the ELO lifetime. Note also in Figure 16 that an important amount of hot gas is outside the spheres of radii r_{vir} , that is, it is not bound to the self-gravitating configuration defined by the ELO halo. In fact, the mass of hot gas increases monotonically up to $r \simeq 4r_{\text{vir}}$, and maybe also beyond this value, but it is difficult at these large radii to properly elucidate whether or not a given hot gas mass element belongs to a given ELO or to another close one (to alleviate this difficulty, only those ELOs not having massive neighbours within radii of $6 \times r_{\text{vir}}$ have been considered to draw this Figure). Another important result is that the hot gas mass fraction, relative to the cold mass fraction at the ELO scale, increases with M_{vir} at given r/r_{vir} , and the differences between massive and less massive ELOs can be as high as a factor of ~ 2 at $r/r_{\text{vir}} < 4$. We see that, in massive ELOs, this excess of baryons in the form of hot gas at the outer parts of their configurations, compensates for the lack of baryons in the form of stars at the ELO scales.

6.4 Total three-dimensional mass density profiles

We now address the issue of the total mass (i.e., baryonic plus dark) density profiles. In Figure 17 they are drawn for ELOs in the SF-A sample (upper panel) as well as for those in the SF-B sample (lower panel). In both cases, the profiles corresponding to ELOs in different mass intervals have been drawn with different line and colour codes. Two important results are that i), they are well fit by power-law expressions $\rho^{\text{tot}}(r) \propto r^{-\gamma}$ in a range of r/r_{vir} values larger than two decades, ii), the slope of the power-law increases with decreasing ELO mass, and, iii) a slight SF effects appears, but only at the very inner regions, with SFB sample ELOs showing a worse fit to a power law than their SFA counterparts. Koopmans et al.

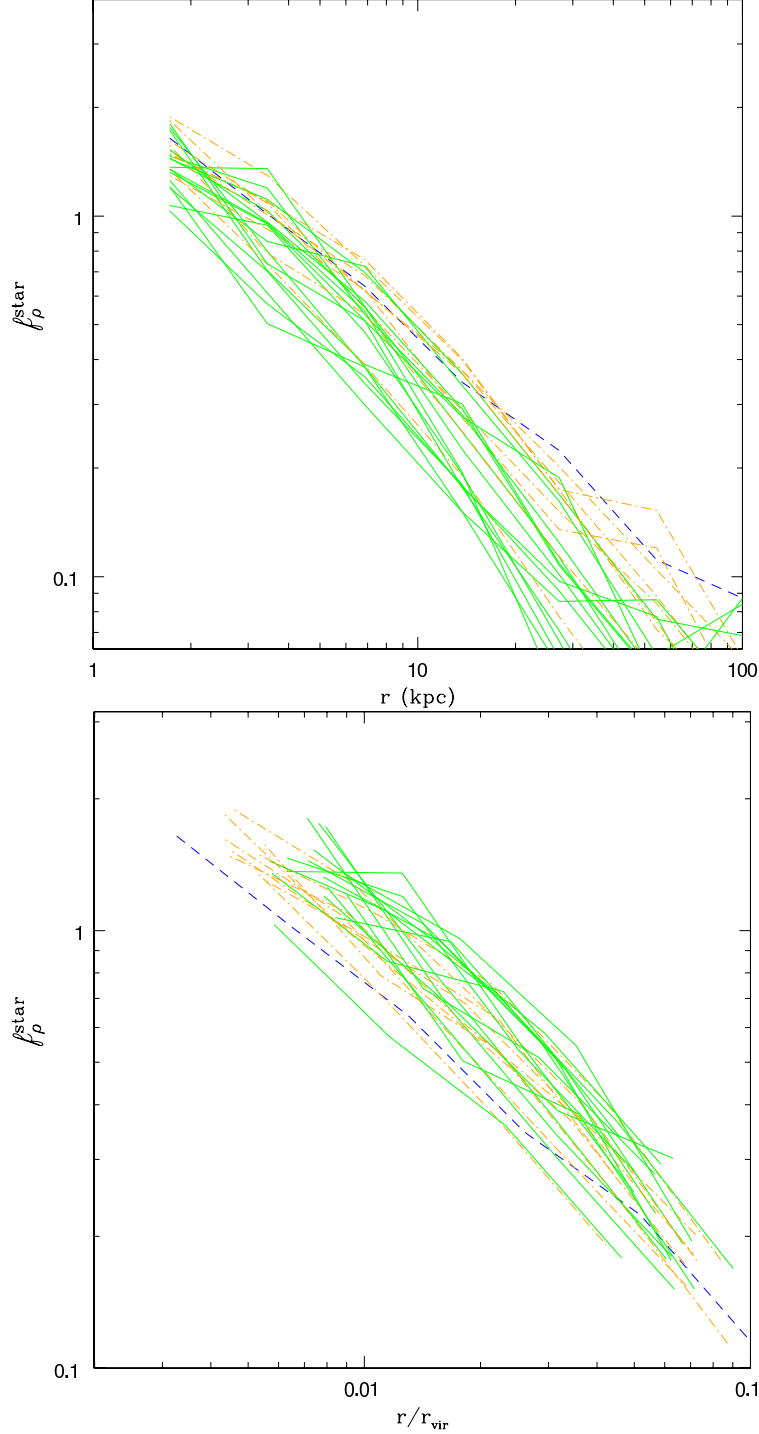


Figure 12. The stellar-to-dark mass profiles for ELOs in the SF-A sample. In the lower panel, radii are normalised to the virial radii. Line types and colours are the same as in Figure 9

2006 have also found that the total mass density profiles of their massive ($\langle \sigma_{\text{ap}} \rangle = 263 \text{ km s}^{-1}$) lens elliptical galaxies can be fit by power-law expressions within their Einstein radii ($\langle R_{\text{Einst}} \rangle = 4.2 \pm 0.4 \text{ kpc}$, with $\langle R_{\text{Einst}}/R_e^{\text{light}} \rangle = 0.52 \pm 0.04$, i.e., the inner region), whose average slope is $\langle \gamma \rangle = 2.01^{+0.02}_{-0.03} \pm 0.05$ (68 percent C.L.), with an intrinsic scatter of 0.12. To elucidate how well the total mass density profiles of ELOs compare with these results, in Figure 18 we plot the slopes γ for ELOs, as well as for SLACS lens ellipticals (Table 1,

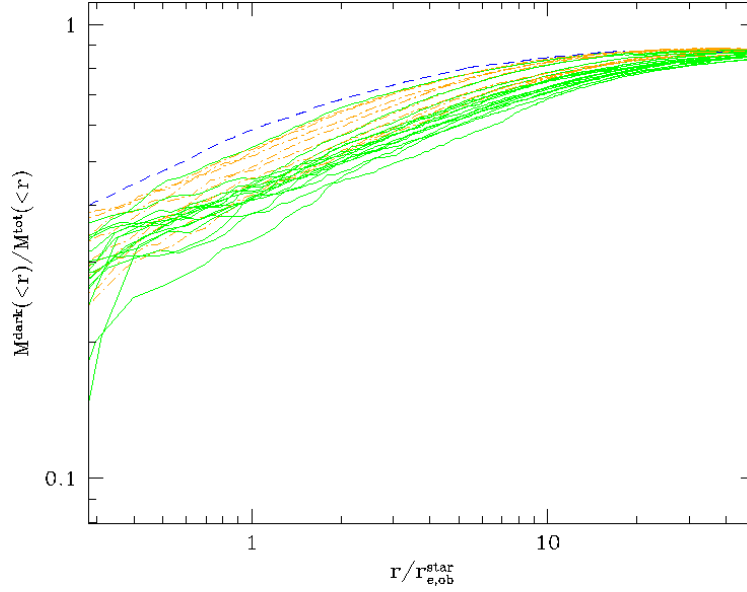


Figure 13. The fraction of dark-to-total mass profiles, $M^{\text{dark}}(<r)/M^{\text{tot}}(<r)$ for ELOs in the SF-A sample; different colours stand for different mass ranges, as in Figure 9; radii are normalised to the 3D stellar half-mass radii

Koopmans et al. 2006), versus their central L.O.S. stellar velocity dispersions. The fitting range for ELOs used to draw this Figure is $r < R_{\text{e,bo}}^{\text{star}}$. We see that results for ELO and SLACS lens galaxy samples are consistent in the range of velocity dispersion values where they coincide.

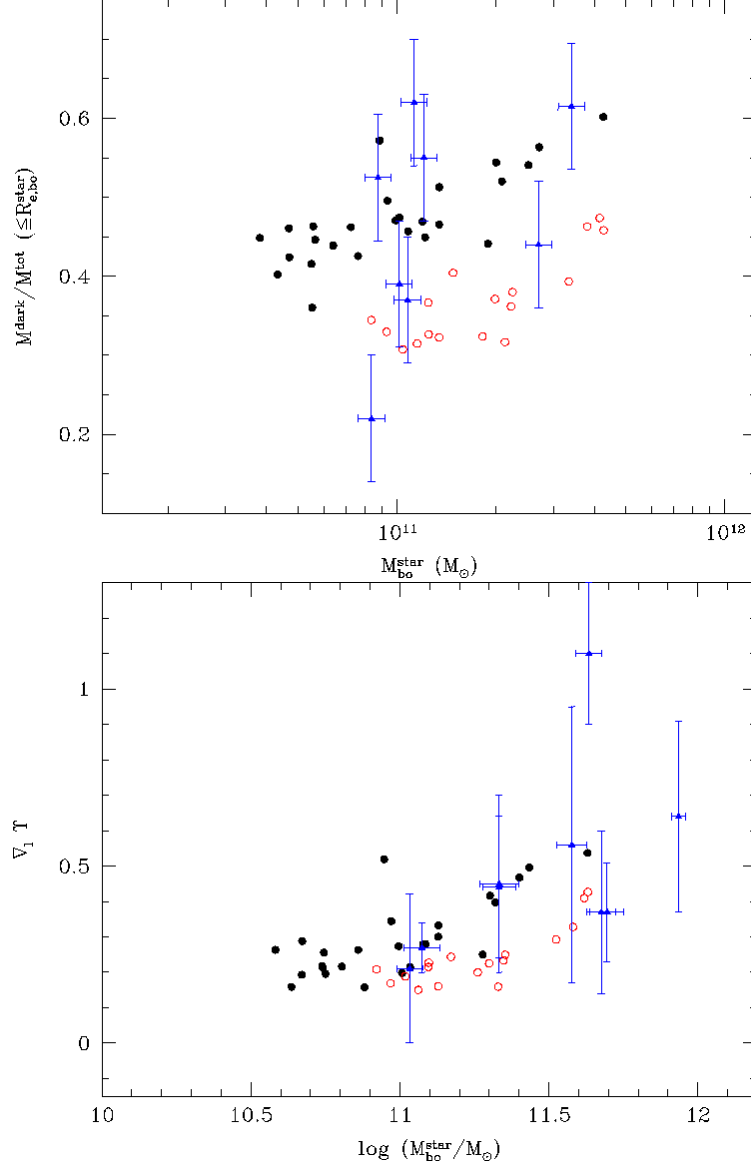


Figure 14. Upper panel: the fraction of dark-to-total mass at $r/R_{\text{e,bo}}^{\text{star}} = 1$ versus the ELO stellar masses. Filled (open) symbols: ELOs in SF-A (SF-B) sample. Points with error bars are the values corresponding to the SAURON sample of ellipticals. Lower panel: the gradients of the $M^{\text{dark}}(< r)/M^{\text{star}}(< r)$ profiles as a function of their stellar masses; blue triangles with error bars are the empirical mass-to-light gradients as determined by Napolitano et al. 2005 for galaxies with the $a_4 \times 100$ shape parameter lower than 0.1 (that is, for boxy ellipticals)

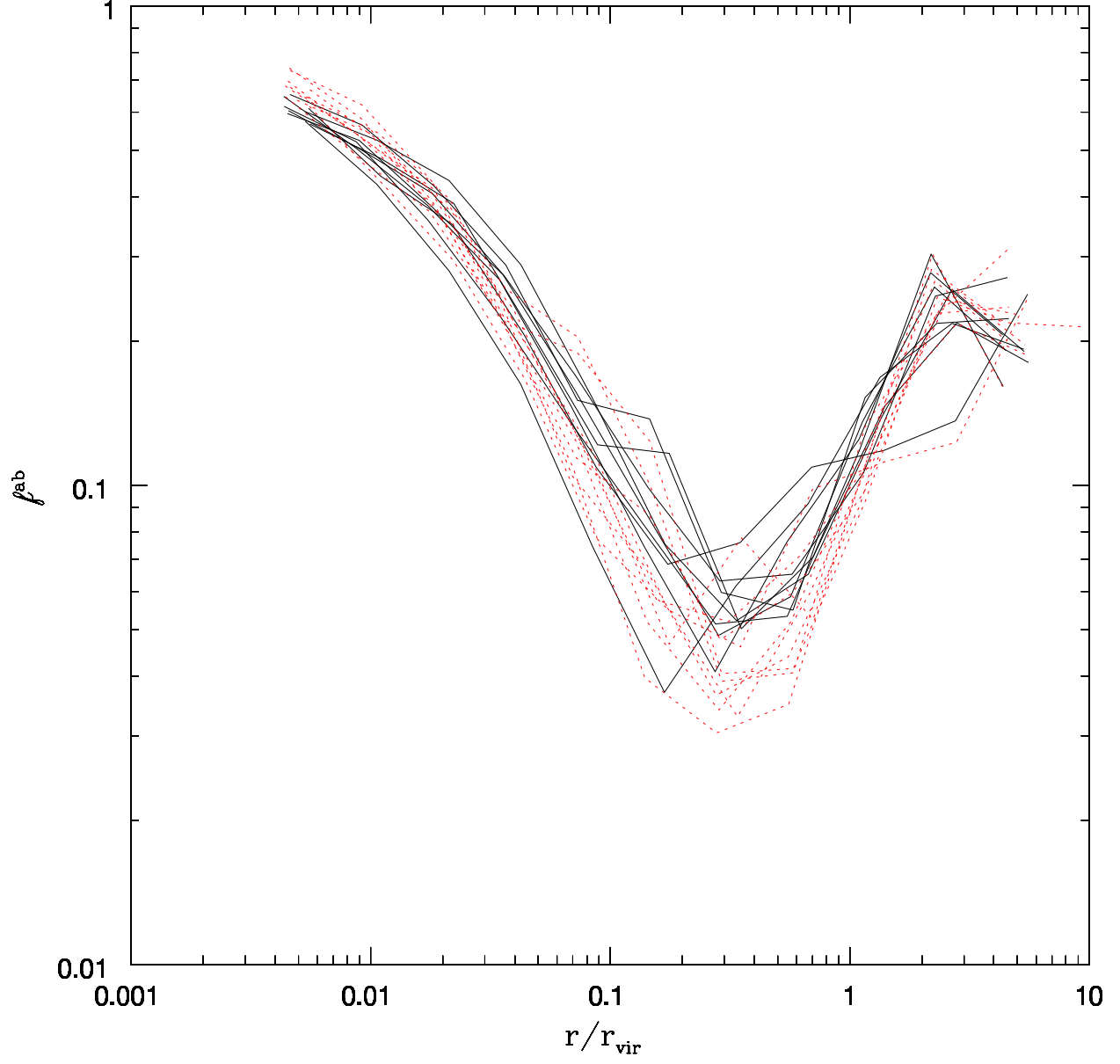


Figure 15. Baryon fraction profiles for ELOs in SF-A sample (black full lines) and SF-B sample (red point lines), in the same range of virial mass, $1.5 \times 10^{12} M_{\odot} \leq M_{\text{vir}} < 5 \times 10^{12} M_{\odot}$

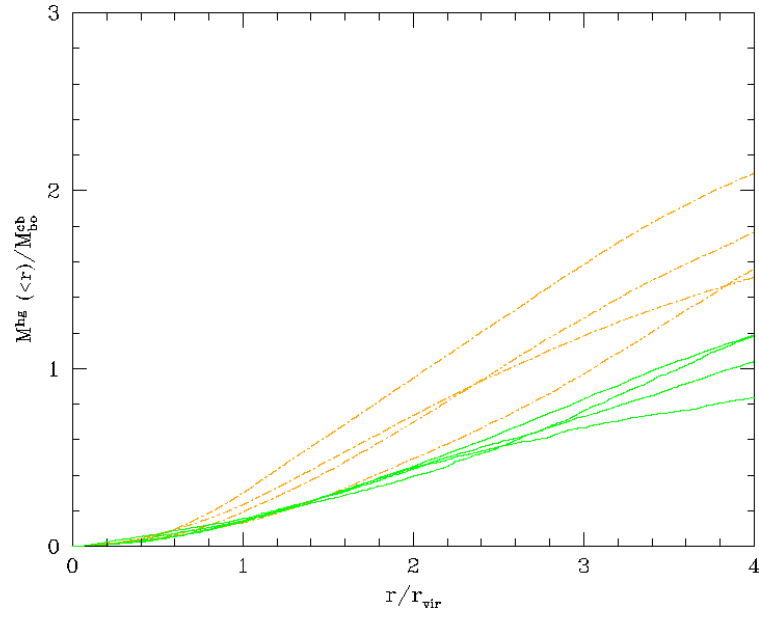


Figure 16. The $M^{\text{hg}}(<r)/M_{\text{bo}}^{\text{cb}}$ profiles for typical ELOs. $M^{\text{hg}}(<r)$ is the mass of hot gas within a sphere of radius r . Orange point-dashed lines: ELOs with $1.5 \times 10^{12} \leq M_{\text{vir}} < 5 \times 10^{12} M_{\odot}$; green full lines: ELOs with $M_{\text{vir}} < 1.5 \times 10^{12} M_{\odot}$. Only isolated ELOs have been considered.

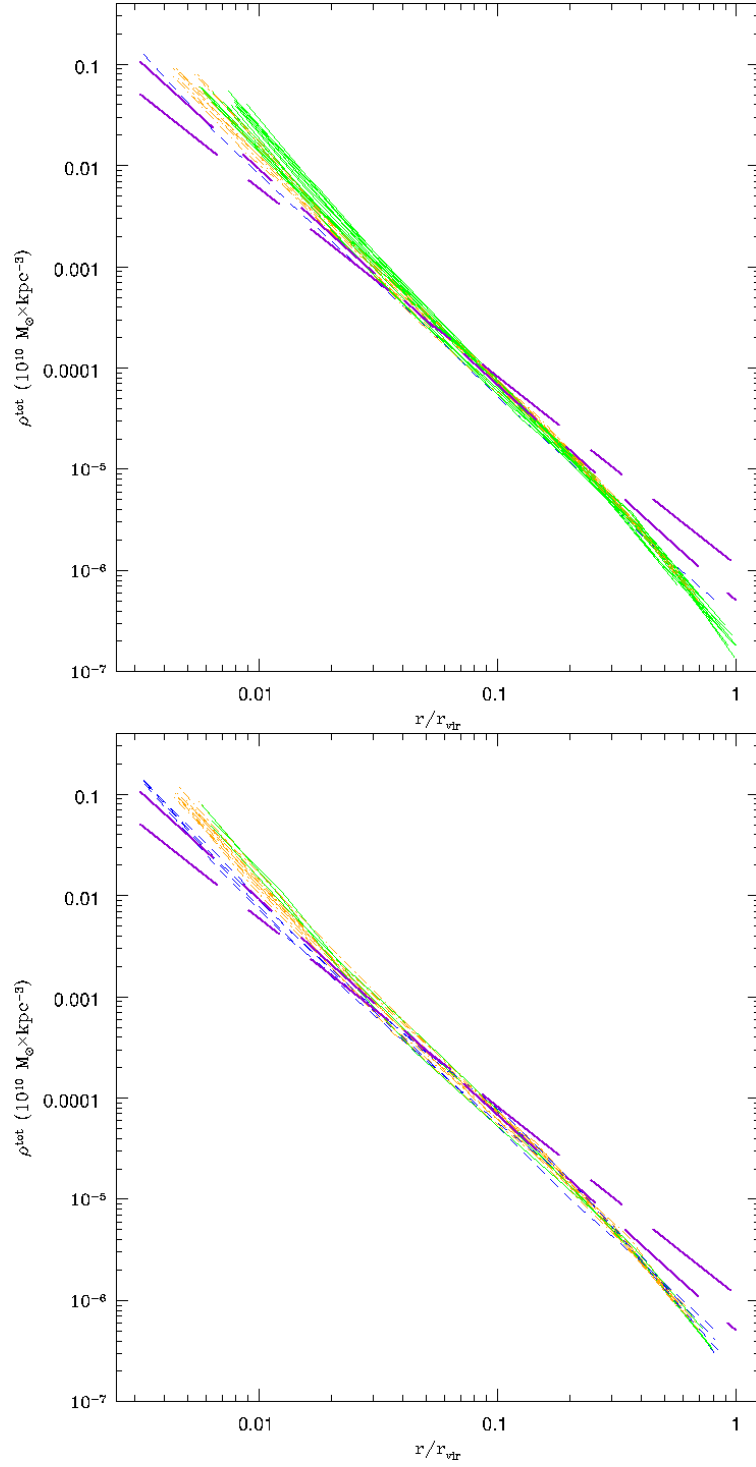


Figure 17. The total mass density profiles for ELOs in the SF-A sample (up) and in the SF-B sample (down). Green full lines: ELOs with $M_{\text{vir}} < 1.5 \times 10^{12} M_{\odot}$; orange point-dashed lines: ELOs with $1.5 \times 10^{12} M_{\odot} \leq M_{\text{vir}} < 5 \times 10^{12} M_{\odot}$; blue dashed lines: ELOs with $5 \times 10^{12} M_{\odot} \leq M_{\text{vir}}$.

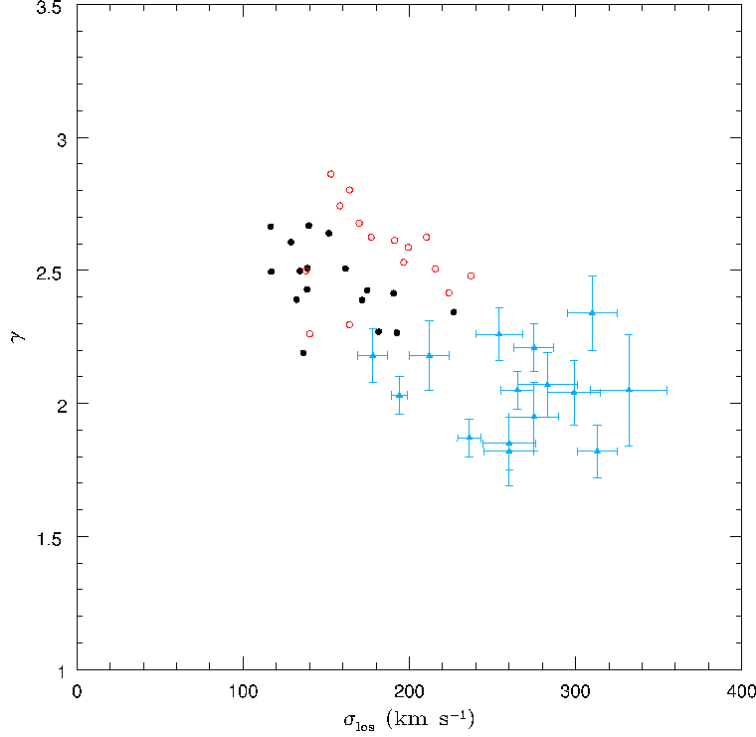


Figure 18. The logarithmic slopes corresponding to the total mass density profiles for ELOs in the SF-A (black filled circles) and the SF-B samples (red open circles), versus their central L.O.S. stellar velocity dispersions. Triangles with error bars correspond to data on SLACS lens ellipticals, as given in Table 1 of Koopmans et al. (2006)

7 KINEMATICS

7.1 Three-dimensional velocity distributions

Shapes and mass density profiles (i.e., positions) are related to the 3D velocity distributions of relaxed E galaxies through the Jeans equation (see Binney & Tremaine 1987). Observationally, informations on such 3D distributions are not available for external galaxies, only the line-of-sight velocity distributions (LOSVD) can be inferred from their spectra (Binney & Tremaine 1987; van der Marel & Franx 1993; de Zeeuw & Franx 1991). The complete six dimensional phase space informations for each of the particles sampling the ELOs provided by numerical simulations, allow us to calculate the 3D profiles for the velocity dispersion, $\sigma_{3D}(r)$, as well as the circular velocity profiles, $V_{\text{cir}}(r)$. In Figure 19 we draw the $V_{\text{cir}}(r)$ profiles (full line), as well as their dark matter (short-dashed line) and baryonic contributions (stars, long-dashed line; stars plus cold gas, point line).

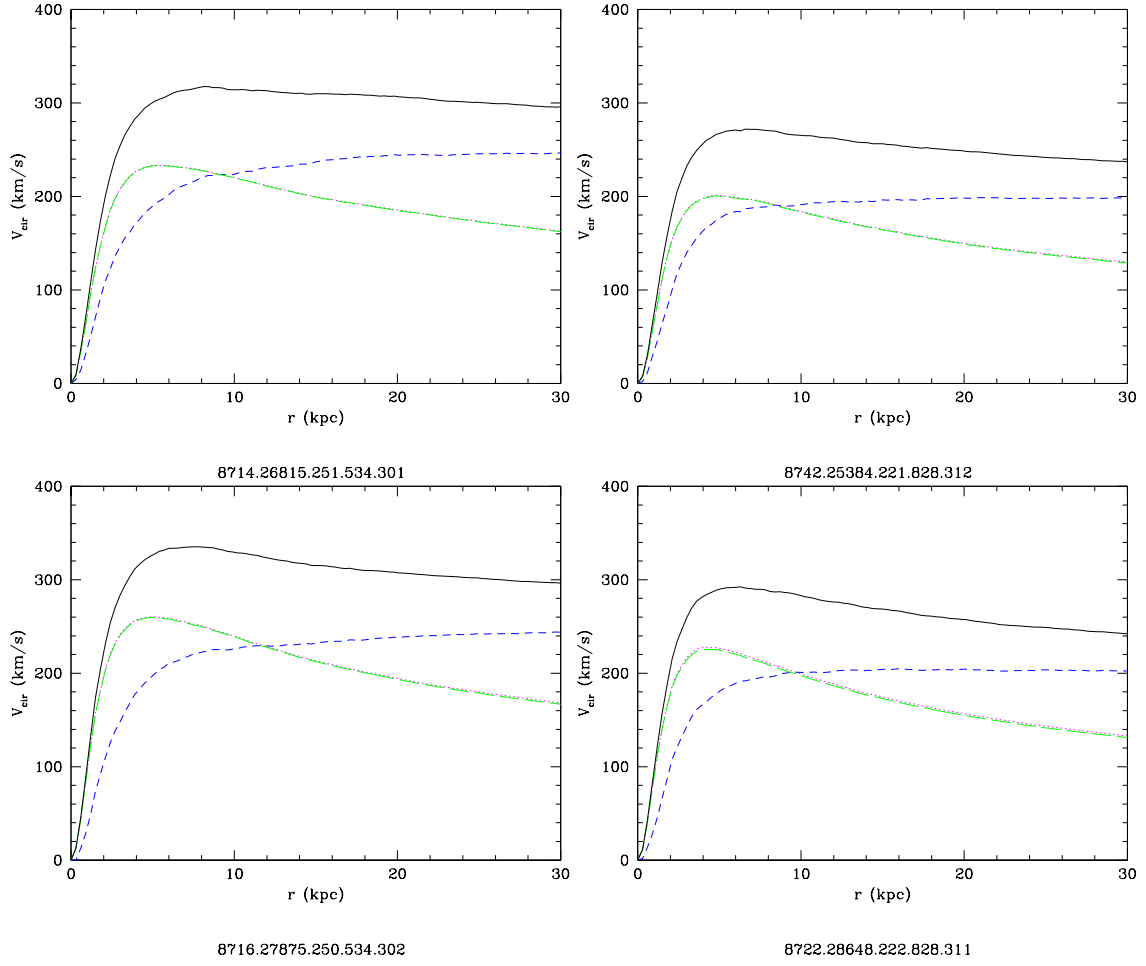


Figure 19. The circular velocities profiles of two typical ELOs in the SF-A sample (upper panels) and their SF-B sample counterparts (lower panels). Black continuous line: total mass; blue short-dashed line: dark matter contribution; green long-dashed line: stellar mass contribution; red point line: cold baryon contribution

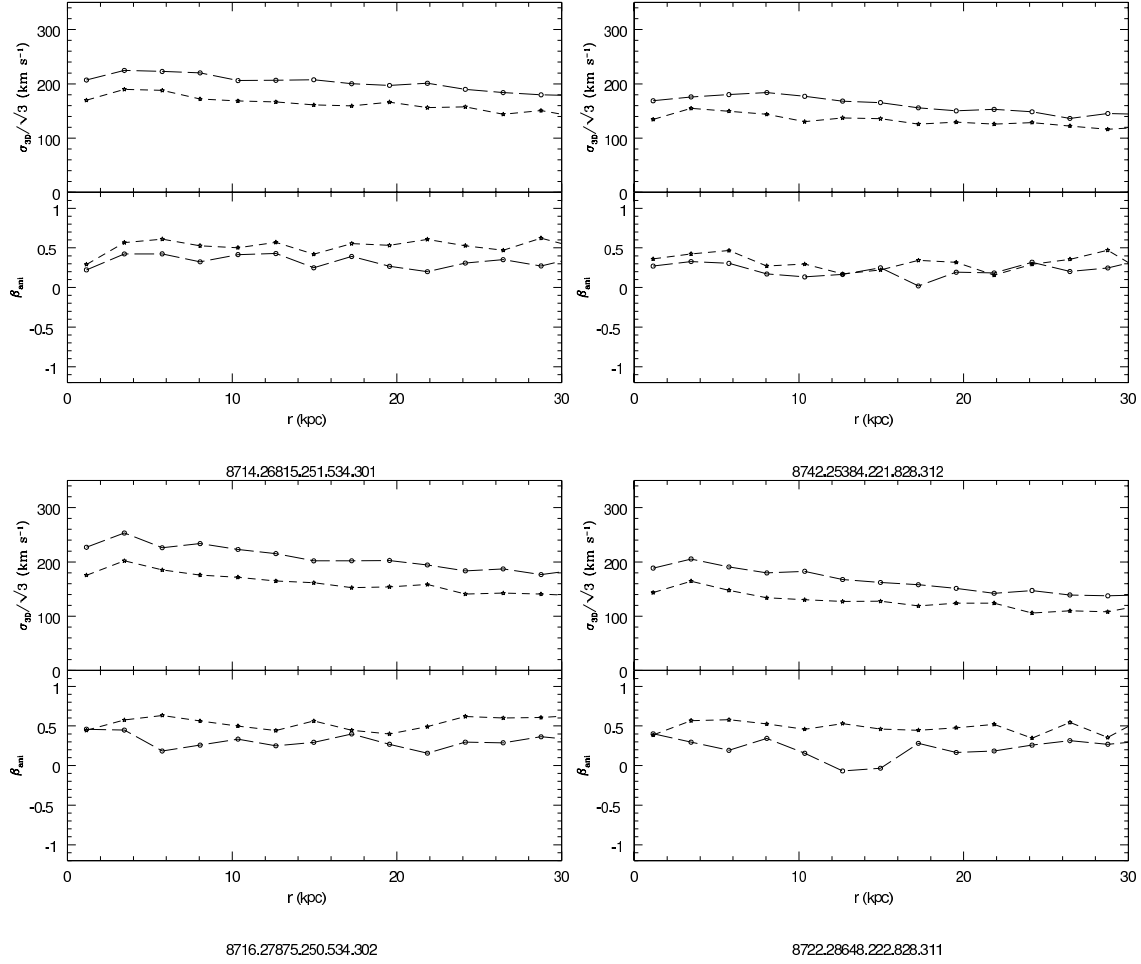


Figure 20. The $\sigma_{3D}(r)$ profiles of two typical ELOs in the SF-A sample (upper panels) and their SF-B sample counterparts (lower panels). Also shown are the anisotropy profiles $\beta_{ani}(r)$. Long-dashed lines: dark matter; short-dashed lines: stars

The $V_{cir}(r)$ profiles provide another measure of ELO mass distribution. We note in Figure 19 that baryon mass distribution is more concentrated than dark matter is, due to energy losses by the gaseous component before being transformed into stars. This is a general property of the circular velocity profiles of the ELO samples. Moreover, objects in SF-B sample are more concentrated than their SF-A sample counterparts, because of the SF implementation: the amount of baryons at their central volumes relative to dark matter is always lower in SF-A than in SF-B objects; this is a small scale effect as $r \sim 30$ kpc or $r \sim 40$ kpc radii enclose roughly similar amounts of baryons or dark matter in any cases.

In Figure 20 we draw the $\sigma_{3D}(r)$ profiles for the same ELOs as measured either by stars, $\sigma_{3D}^{star}(r)$ (starred symbols and short-dashed lines), and dark matter, $\sigma_{3D}^{dark}(r)$ (open circles and long-dashed lines) particles as proof particles in the overall potential well. These profiles are in any case decreasing outwards, both for dark matter or stellar components. An outstanding result illustrated by Figure 20 is that $\sigma_{3D}^{dark}(r)$ is always higher than $\sigma_{3D}^{star}(r)$ (because stars are made out of cooled gas), with $\sigma_{3D}^{star}(r)/\sigma_{3D}^{dark}(r) \sim 0.8$, in consistency with the values found by Loewenstein (2000) on theoretical grounds and by Dekel et al. (2005) from pre-prepared simulations of mergers of disk galaxies. This is the so-called kinematical segregation (Sáiz 2003, Sáiz et al. 2004). To further analyse this issue, in Figure 21 we plot the $\sigma_{3D}^{star}(r)/\sigma_{3D}^{dark}(r)$ ratios for the ELOS in both the SF-A sample and in the SF-B sample, with different colour and line codes depending on the ELO mass range. We see that the kinematical segregation

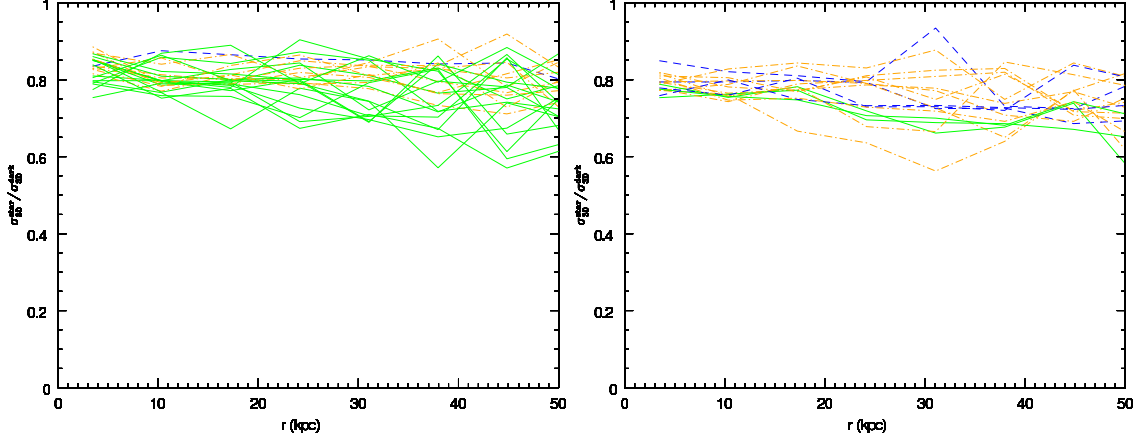


Figure 21. The $\sigma_{3D}^{\text{star}}(r)/\sigma_{3D}^{\text{dark}}(r)$ ratio profiles for ELOs in SF-A (upper panel) and SF-B (lower panel) samples. Different colour and line codes stand for ELO mass intervals, as in Figure 9

does not show neither a clear mass dependence, nor a radial dependence. Moreover, the SF parametrisation effect is only mild.

Another relevant quantity is the anisotropy of the 3D velocity distributions of the ELO sample, defined as:

$$\beta_{\text{ani}} = 1 - \frac{\sigma_t^2}{2\sigma_r^2}, \quad (15)$$

where σ_r and σ_t are the radial and tangential velocity dispersions ($\sigma_t^2 = \sigma_\theta^2 + \sigma_\phi^2$), relative to the centre of the object. The anisotropy profile, $\beta_{\text{ani}}(r)$, is represented in Figure 20 for typical ELOs in the sample, for their dark matter and stellar particle components. The anisotropy is always positive (i.e., an excess of dispersion in radial motions), the profiles are almost constant, except at the innermost regions, and the stellar component is always more anisotropic than the dark matter one, presumably as a consequence of the mergers involved in the ELO mass assembly (see §4 and DTal06). In fact, the characteristics of the stellar anisotropy profiles (roughly constant and $\beta_{\text{ani}}^{\text{star}}(r) \simeq 0.5$ in most cases) are consistent with those found by Dekel et al. (2005), where they conclude that large radial anisotropy is generic to the stellar component of merger remnants of any kind.

7.2 Stellar LOS velocity and velocity dispersion profiles

The two last Figures provide an illustration of the general characteristics of the lower-order moments of the 3D velocity distribution. The profiles plot in these Figures are not observationally available, but only the lower-order moments of the LOSVD are. We have measured the stellar line-of-sight velocity and the stellar velocity dispersion profiles, $V_{\text{los}}^{\text{star}}(R)$ and $\sigma_{\text{los}}^{\text{star}}(R)$, along three orthogonal projections for all ELOs in the sample. To mimic observational techniques used in stellar kinematics of elliptical galaxies, we have measured these profiles along the major and minor axes of projected ELOs, where the major axis is defined as that orthogonal to the ELO spin vector projected on the plane normal to the LOS, and the minor axis is parallel to the spin projection. We have found that in some cases ELOs do indeed show a clear rotation curve, while in most cases the rotation is only modest or even very low, as illustrated in Figure 22 and in Figure 23, respectively.

To quantify the amount of rotation in ELOs and its possible dependence on the mass scale, in Figure 24 we plot the ratios $c_{\text{rot}} = V_{\text{min}}/(V_{\text{maj}}^2 + V_{\text{min}}^2)^{1/2}$ as a function of the ELO

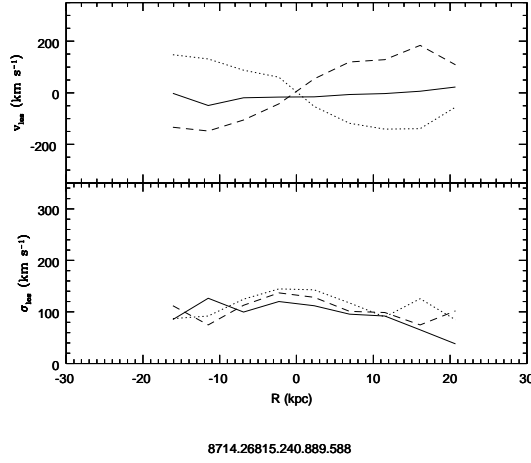


Figure 22. Upper panel, full line: the major axis stellar LOS velocity profile along the spin direction for an ELO in SF-A sample. Point and dashed lines: same as the continuous line taking the LOS direction normal to the ELO spin vector. This particular ELO rotates. Lower panel: same as the upper panel for the major axis LOS stellar velocity dispersion profiles

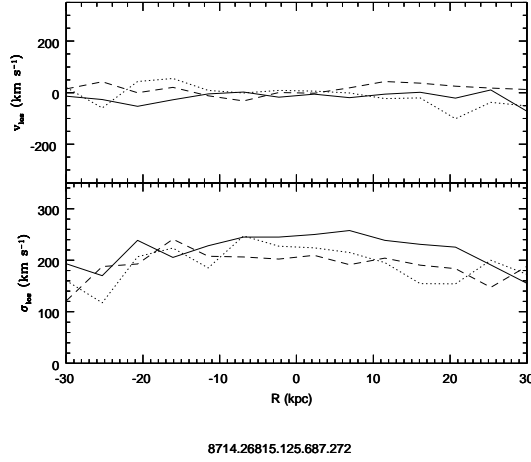


Figure 23. Same as the previous Figure for another ELO. In this case, the rotation is only mild.

virial masses, for ELOs in both the SF-A and the SF-B samples (V_{maj} and V_{min} are the maximum values of the $V_{\text{los}}^{\text{star}}(R)$ profile when measured along the major and the minor axes, respectively). When the ELO shows a clear rotation curve, V_{min} is much lower than V_{maj} , and the c_{rot} ratio is low; by contrast, when the rotation is unimportant, then $V_{\text{min}} \simeq V_{\text{maj}}$ and $c_{\text{rot}} \sim 0.7$. For a given ELO, the c_{rot} value depends on the direction taken as LOS direction, in such a way that it is maximum when the ELO spin is taken as LOS direction, and minimum when the LOS direction is normal to the ELO spin vector, that is, when rotation stands out. This is the LOS direction taken to draw this Figure, where we see that there is not a clear mass dependence, that most ELOs are in between the two situations

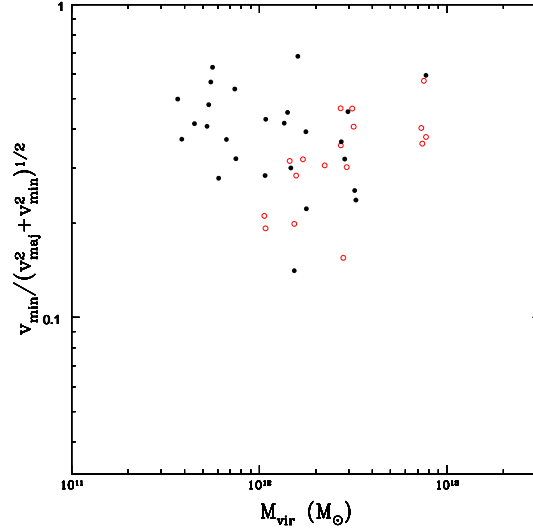


Figure 24. The c_{rot} ratios as a function of the virial mass for ELOs in the samples

described above and that the values of the c_{rot} ratio of ELOs are typical of boxy ellipticals (see, for example, Binney & Merrifield, figure 4.39).

We now comment on the major axis LOS stellar velocity dispersion profiles of ELOs (Figure 22 and in Figure 23). Their most outstanding feature is the decrease of the $\sigma_{\text{los}}^{\text{star}}(R)$ profiles show in some cases and particularly so along some LOS directions at large R . These profiles are suited to compare with stellar kinematics data. In other cases, for example to compare with planetary nebulae data, the LOS velocity dispersion profiles must be calculated by averaging over the LOS velocities of stars placed within cylindrical shells, with their axes in the LOS direction. Figure 25 is a plot of such profiles normalised to $\sigma_{\text{los}}^{\text{star}}(R_{\text{e,bo}}^{\text{star}})$ for the SF-A sample ELOs; each panel corresponds to a different orthogonal projection.

To make clearer the decline of the $\sigma_{\text{los}}^{\text{star}}(R)$ profiles, in Figure 26 we plot, at different R values, the averages of the stacked profiles shown in Figure 25 with their dispersions (green points and error bars), as well as the averages of the profiles corresponding to young stars (age ≤ 3 Gyears, orange squares and error bars), normalised for each ELO to their corresponding $\sigma_{\text{los}}^{\text{star}}(R_{\text{e,bo}}^{\text{star}})$. The decline of these velocity dispersion profiles can be clearly appreciated, as well as the slightly larger decline of the profiles corresponding to the younger stellar populations. These results are consistent, within their dispersions, with that shown by Dekel et al. (2005) in their figure 2 (lower panel). They are also marginally consistent with the decline shown by PN data in the NGC 821, NGC 3379, NGC 4494 and NGC 4697 galaxies (Romanowsky et al. 2003; Romanowsky 2006). Note, however, that our ELOs are boxy, while the $a_4 \times 100/a$ shape parameters for these galaxies are 2.5, 0.2, 0.3 and 1.4, respectively, that is, they are rather disk ellipticals.

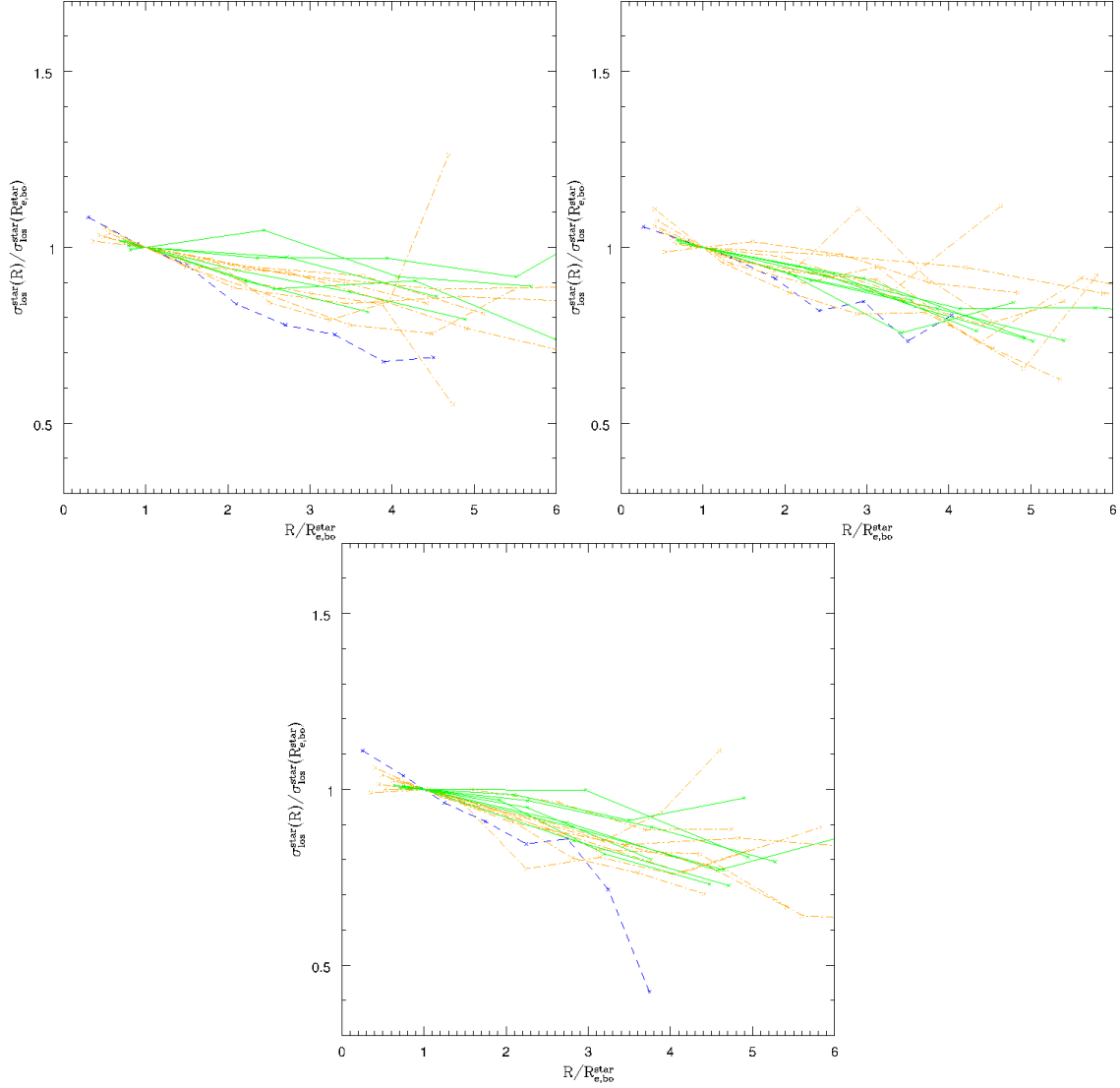


Figure 25. LOS velocity dispersion velocity profiles along three different orthogonal projections for ELOs in SF-A sample up to 6 effective radii. The profiles are normalised to their value at $R_{e,bo}^{star}$ for each ELO. Different colour and line codes stand for ELO mass intervals, as in Figure 9

8 SUMMARY, DISCUSSION AND CONCLUSIONS

8.1 Summary: method and main results

This paper belongs to a series aimed at studying galaxy formation in a cosmological context through hydrodynamical simulations. Here we present an analysis of the sample of elliptical-like-objects (ELOs) formed in ten different cosmological simulations, run within the same global flat Λ cosmological model, roughly consistent with observations. The normalisation parameter has been taken slightly high, $\sigma_8 = 1.18$, as compared with the average fluctuations of 2dFGRS or SDSS galaxies to mimic an active region of the Universe. Newton laws and hydrodynamical equations have been integrated in this context, with a standard cooling algorithm and a star formation parameterisation through a Kennicutt-Schmidt-like law, containing our ignorance about its details at sub-kpc scales, and where subresolution processes affecting star formation are implicitly taken into account through the values given to these parameters. No further hypotheses to model the assembly processes have been made.

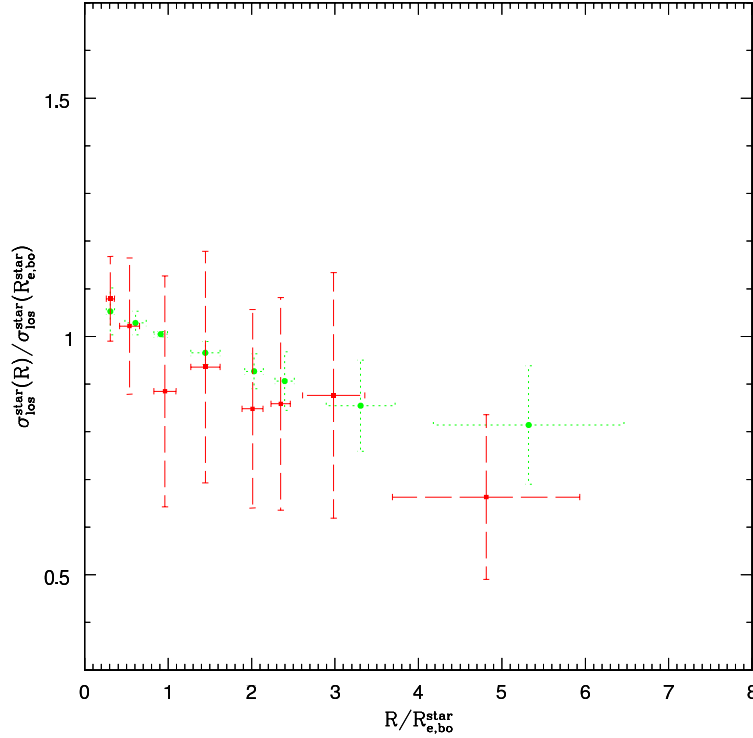


Figure 26. The SFA sample average LOS velocity dispersion profiles normalised to their values at $R_{e,bo}^{star}$ for each ELO (green points) along with their 1σ dispersions. Orange points and error bars: the same for the young stellar particles, with the same normalisation

Individual galaxy-like objects naturally appear as an output of the simulations, so that the physical processes underlying mass assembly can be studied. Five out of the ten simulations (the SF-A type simulations) share the SF parameters and differ in the seed used to build up the initial conditions. To test the role of SF parameterisation, the same initial conditions have been run with different SF parameters making SF more difficult, contributing another set of five simulations (the SF-B type simulations). ELOs have been identified in the simulations as those galaxy-like objects at $z = 0$ having a prominent, dynamically relaxed spheroidal component made out of stars, with no extended discs and very low gas content. This stellar component is embedded in a dark matter halo that contributes an important fraction of the mass at distances from the ELO centre larger than $\sim 10 - 15$ kpc on average, within which some clumps made out of cold dense gas and stars, associated in some cases with dark matter substructures, orbit. No ELOs with stellar masses below $3.8 \times 10^{10} M_{\odot}$ or virial masses below $3.7 \times 10^{11} M_{\odot}$ have been found that met the selection criteria (see Kauffmann et al. 2003 for a similar result in SDSS galaxies and Dekel & Birnboim 2006, and Cattaneo et al. 2006 for a possible physical explanation). ELOs have also an extended halo of hot, diffuse gas. Stellar and dark matter particles constitute a dynamically hot component with an important velocity dispersion, and, except in the very central regions, a positive anisotropy.

The first step in the program of studying the origins of elliptical galaxies through self-consistent simulations, is to make sure that they produce ELO samples that have counterparts in the real local Universe. This objective has been partially fulfilled in previous works. An analysis of the structural and dynamical ELO parameters that can be constrained from observations has shown that they are consistent with those measured in the SDSS DR1 elliptical sample (Sáiz et al. 2004), including the FP relation (Oñorbe et al. 2005; Oñorbe

et al. 2006). Also, ELO stellar populations have age distributions with the same trends as those inferred from observations, i.e., most stars have formed at high z on short timescales, and, moreover more massive objects have older means and narrower spreads in their stellar age distributions than less massive ones (DSS04).

In this paper we address the important issue of the amount and distribution of dark matter in virtual ellipticals and, in particular, its amount and distribution relative to the bright matter distribution. We also address the kinematics of the dark matter component and its relationship with the kinematics of the bright matter component. We want to answer to the question of the mass and extension of dark matter haloes in elliptical galaxies. To answer to this question, we have first compared our virtual results with new observational data, obtaining a very satisfactory agreement. To be specific:

- The projected stellar *mass* profile, $\Sigma^{\text{star}}(R)$, can be adequately fitted by a Sérsic-like law. The shape parameter values n we have obtained are consistent with observations, including their correlations with the ELO luminosity, size and velocity dispersion.
- The fraction of dark-to-total mass inside the projected half-mass radii are consistent with the observational ones obtained by Cappellari et al. (2006) from SAURON data.
- The gradients of the dark-to-stellar $M^{\text{dark}}(< r)/M^{\text{star}}(< r)$ profiles as a function of their stellar masses, are consistent with those observationally found by Napolitano et al. (2005) for boxy ellipticals.
- The total mass (i.e., baryonic plus dark) density profiles can be well fit by a power-law expression in a large range of r/r_{vir} values, with power-law slopes that are consistent with, within the dispersion, or slightly higher than those observationally found by Koopmans et al. 2006 for massive lens ellipticals within their Einstein radii.
- The line-of-sight velocity profiles along the major axis show, in some cases, a clear rotation, even if in most cases the rotation is modest or low. The values of the rotation ratio along the major and minor axis (a measure of the rotation in ELOs) does not depend on the mass scale
- The values spanned by the rotation ratios of ELOs are typical of boxy ellipticals.
- The line-of-sight velocity dispersion profiles, $\sigma_{\text{los}}(R)$, decline outwards at large R , and the slope slightly increases when only the younger stellar populations are considered. These profiles are only marginally consistent with data on PNs at large radii; but these correspond to disk ellipticals while our virtual ellipticals are rather boxy.

These agreements strongly suggest that the intrinsic three-dimensional dark and bright matter mass and velocity distributions we get in our simulations might also adequately describe real ellipticals. We now summarise our most important findings on the three-dimensional mass and velocity structure of ELOs:

- ELOs are embedded in extended massive dark matter haloes.
- The best fits of their spherically-averaged dark matter density profiles to usual analytical formulae (Hernquist 1990; Navarro et al. 1995, 1996; Tissera & Domínguez-Tenreiro 1998; Jing & Suto 2000 (JS) and Navarro et al. 2004 (Nav04)) are generally provided by the two last formulae. The quality of the fits is good, so that ELO haloes, in consistency with those produced in purely N-body simulations, form a two-parameter family where the two parameters are correlated. The JS inner slope parameter, α , is always higher than the NFW value ($\alpha=1$).
- The slope parameters grow as the ELO mass scale decreases, indicating that the halo concentration grows when the mass decreases.
- Halos have suffered from adiabatic contraction. This can be made quantitative by com-

paring the plot of the density at the Nav04 scale, ρ_{-2} , versus the scale $r_{-2} = a_h$, with the plot provided by Nav04 (results of purely N-body simulations).

- At the ELO scale, most baryons have turned into stars. The three dimensional stellar-mass density profiles can be fit by Nav04 or JS profiles, but with small r_{-2} values.

- The mass distribution homology is broken in the stellar mass as well as in the dark-versus bright-mass distributions, with the stellar mass distribution relative to dark mass one less concentrated with increasing ELO mass. That is, massive ELOs miss baryons at short scales as compared with less massive ones, when we normalise to the dark matter content. This result is consistent with the observational ones by Cappellari et al. (2006) from SAURON data, as well as by Napolitano et al. (2005) we quoted above.

- At the halo scale, the baryon fraction profiles have been found to show a typical pattern, where their values are high at the centre, then they decrease and have a minimum roughly at $0.3 < r_{\min}^{\text{ab}}/r_{\text{vir}} < 0.7$, well below the global value, $\Omega_b/\Omega_m = 0.171$, then they increase again, reach a maximum value and then they decrease and fall to the global Ω_b/Ω_m value well beyond the virial radii r_{vir} . This suggests that the baryons massive ELOs miss at short scales (stars) are found at the outskirts of the configuration as diffuse hot gas. This result could reflect the presence of a stable virial shock that prevents gas infall more efficiently as mass increases (Dekel & Birnboim 2006).

- Concerning kinematics, ELO velocity dispersion profiles in three dimensions are slightly decreasing for increasing r , both for dark matter and stellar particles, $\sigma_{3D}^{\text{d}}(r)$ and $\sigma_{3D}^{\text{star}}(r)$.

- The dark and bright matter components of ELOs are kinematically segregated, as we have found that $(\sigma_{3D}^{\text{d}}(r))^2 \sim (1.4 - 2) (\sigma_{3D}^{\text{star}}(r))^2$, confirming previous results (Sáiz 2003; Loewenstein 2000; Dekel et al. 2005). This is so because stars are formed from gas that had lost energy by cooling.

- This kinematical segregation does not show any clear mass or radial dependence.

- The anisotropy is always positive (i.e., an excess of radial motions) and almost non-varying with r inside the ELOs. Recall, however, that ELOs have been identified as dynamically relaxed objects: there are not recent mergers in our samples.

- The stellar component generally shows more anisotropy than the dark component, maybe derived from the radial motion of the gas particles that gave rise to the stars.

8.2 Possible resolution effects

To make sure that the results we report in this paper are not unstable under resolution changes, a control simulation with 128^3 dark matter and 128^3 baryonic particles, a gravitational softening of $\epsilon = 1.15$ kpc and the other parameters as in SF-A type simulations (the S128 simulation), has been run. The results of its analysis have been compared with those of a 2×64^3 simulation (the S64 simulation), whose initial conditions have been built up by randomly choosing 1 out of 8 particles in the S128 initial conditions, so that every ELO in S128 has a counterpart in the lower resolution simulation and conversely. Due to the very high CPU time requirements for S128, the comparison has been made at $z = 1$. The results of this comparison are very satisfactory, as Figure 27 illustrates.

Otherwise, Figures 20 and 21 show that two-body relaxation effects (typically the most stringent requirement for convergence) have not been important at least for r larger than ~ 1 kpc. In fact, two-body relaxation effects cause energy equipartition. But the the values of the $\sigma_{3D}^{\text{star}}(r)/\sigma_{3D}^{\text{dark}}(r)$ ratios we have obtained ($\simeq 0.8$) exclude energy equipartition among dark matter and stellar particles in ELOs, because such equipartition would demand $\sigma_{3D}^{\text{star}}(r)/\sigma_{3D}^{\text{dark}}(r) = [m^{\text{dark}}/m^{\text{star}}]^{0.5} = 2.194$, where $m^{\text{dark}} = 1.29 \times 10^8 M_{\odot}$ and $m^{\text{star}} = 2.67 \times 10^7 M_{\odot}$ are the mass of dark and stellar particles, respectively. This result is impor-

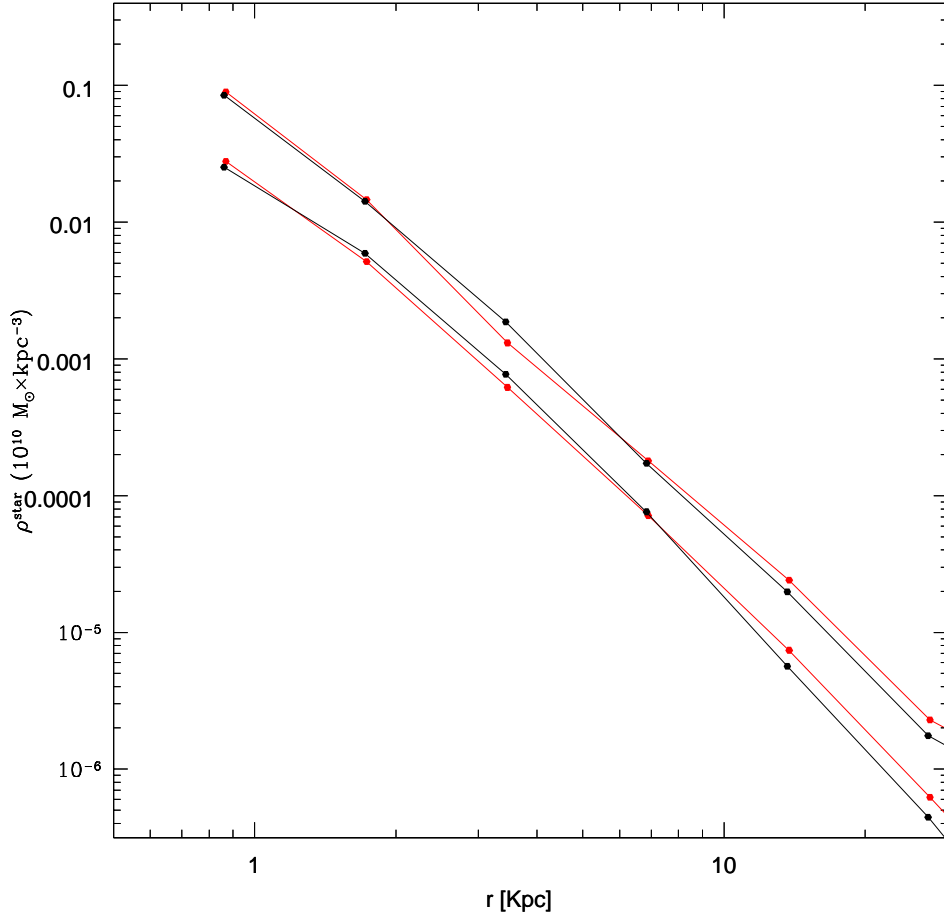


Figure 27. Three-dimensional stellar mass density profiles for 2 ELOs identified at $z = 1$ in S128 (red lines) and their counterparts in S64 (black lines).

tant because it shows that two-body relaxation effects have played no important role in the gravitational interaction.

8.3 The physical processes underlying mass homology breaking and their observational implications

One of the most important findings of this paper is the homology breaking ELO samples show both in their relative content and relative distributions of the baryonic and the dark mass components. As explained in Oñorbe et al. (2005, 2006), this has as a consequence the observed tilt of the Fundamental Plane relation relative to the virial one. Which are the physical processes underlying this breaking of homology? According with our simulations, they lie in the systematic decrease, with increasing ELO mass, of the relative amount of dissipation experienced by the baryonic mass component along ELO stellar mass assembly (DTal06; Oñorbe et al., in preparation). This possibility, already suggested by Bender, Burstein & Faber (1992), Guzmán, Lucey & Bower (1993) and Ciotti, Lanzoni & Renzini (1996), was first addressed through numerical methods by Bekki (1998). He studied elliptical formation through pre-prepared simulations of dissipative mergers of disk galaxies, where the rapidity of the star formation in mergers is controlled by a free efficiency parameter

C_{SF} . He shows that the star formation rate history of galaxies determines the differences in dissipative dynamics, so that to explain the lack of homology in elliptical galaxies he *needs to assume* that more luminous galaxies are formed by galaxy mergers with a shorter timescale for gas transformation into stars. Recently, Kobayashi (2005) and Robertson et al. (2006) have confirmed the importance of dissipation and the timescale for star formation to explain mass homology breaking in ellipticals.

In this paper we go an step further and study mass and velocity distributions of two samples of virtual ellipticals formed in self-consistent cosmological simulations. As explained in Section 3, the simulations provide us with clues on the physical processes involved in elliptical formation. They indicate that most of the dissipation involved in the mass assembly of a given ELO occurs in the violent early phase at high z and on very short timescales (and earlier on and on shorter timescales as the ELO mass grows, see details in DSS04 and DTal06), as a consequence of ELO assembly out of gaseous material and its transformation into stars. Moreover, the dissipation rate history is reflected by the star formation rate history. During the later slower phase of mass assembly, ELO stellar mass growth essentially occurs without any dissipation and the star formation rate substantially decreases (see more details and Figure 1 in DTal06). So, the mass homology breaking appears in the early, violent phase of mass assembly and it is essentially preserved during the later, slower phase. A consequence is that the dynamical plane appears in the violent phase and is roughly preserved along the slower phase, see discussion in DTal06.

We see that our results on the role of dissipative dynamics essentially include previous ones, but they also add important new informations. First, our results on the role of dissipative dynamics to break mass homology agree with the previous ones, but it is important to note that, moreover, ELO stellar populations show age effects, that is, more massive objects produced in the simulations *do have* older means and narrower spreads in their stellar age distributions than less massive ones (see details DSS04); this is equivalent to downsizing (Cowie et al. 1996) and naturally appears in the simulations, so that it need not be considered as an additional assumption. Second, the preservation of the dynamical plane in the slow phase of mass aggregation in our simulations also agrees with previous work based on dissipationless simulations of pre-prepared mergers (Capelato et al. 1995; Dantas et al. 2003; González-García & van Albada 2003; Nipoti et al. 2003; Boylan-Kochin et al. 2005). But, again, it is important to note that the important decrease of the dissipation rate in the slow phase of evolution naturally appears in the simulations and we do not have to assume this decrease. Also, the decrease of the merger rate in the later phase of mass assembly results from the global behaviour of the merger rate history in the particular cosmological context we have considered. Third, it turns out that the physical processes involved in ELO formation unveiled by our simulations, not only explain mass homology breaking (and its implications in the formation and preservation of the dynamical plane), and stellar age effects or downsizing in ellipticals, but they might also explain other elliptical properties recently inferred from observations (for example, the appearance of blue cores, Menanteau et al. 2004; the increase of the stellar mass contributed by the elliptical population since higher z , Bell et al. 2004; Conselice, Blackburne, & Papovich 2005; Faber et al. 2005; see more details in DTal06).

8.4 Conclusions

We conclude that the simulations provide an unified scenario where most current observations on ellipticals can be interrelated. In particular, this scenario proofs the importance of dark matter haloes in relaxed virtual ellipticals, and suggests that real ellipticals must

also have extended, massive dark matter haloes. Also, this scenario explains the homology breaking in the relative dark- to bright-mass content and distribution of ellipticals, that could have important implications to explain the physical origin of the Fundamental Plane relation and its preservation. It is worth mentioning that this scenario shares some characteristics of previously proposed scenarios, but it has also significant differences, mainly that most stars in elliptical galaxies form out of cold gas that had never been shock heated at the halo virial temperature and then formed a disk, as the conventional recipe for galaxy formation propounds (see discussion in Keres et al. 2005 and references therein). The scenario for elliptical formation emerging from our simulations has the advantage that it results from simple physical laws acting on initial conditions that are realizations of power spectra consistent with observations of CMB anisotropies.

We thank H. Artal for computing assistance. This work was partially supported by the MCyT (Spain) through grants AYA-0973, AYA-07468-C03-02 and AYA-07468-C03-03 from the PNAyA, and also by the regional government of Madrid through the ASTROCAM Astrophysics network (S-0505/ESP-0237). We thank the Centro de Computación Científica (UAM, Spain) for computing facilities. AS thanks FEDER financial support from UE.

REFERENCES

- Ballesteros-Paredes J., Klessen R. S., McLow M. -M., Vázquez-Semadeni E., 2006, astro-ph/0603357 preprint
 Bekki K., 1998, *ApJ*, 496, 713
 Bell E. F., et al. 2004, *ApJ*, 608, 752
 Bender R., Burstein D., Faber S. M., 1992, *ApJ*, 399, 462
 Bergond G., Zepf S. E., Romanowsky A. J., Sharples R. M., Rhode K. L., 2006, *A&A*, 448, 155
 Bernardi M., et al., 2003, *AJ*, 125, 1866
 Bertin G., Ciotti L., Del Principe M., 2002, *A&A*, 386, 149
 Binney J., Tremaine S., 1987, *Galactic Dynamics*, Princeton University Press (Princeton, New Jersey)
 Binney J., Merrifield M., 1998, *Galactic Astronomy*, Princeton University Press (Princeton, New Jersey)
 Blumenthal G. R., Faber S. M., Flores R., Primack J. R., 1986, *ApJ*, 301, 27
 Bond J. R., Centrella J., Szalay A. S., Wilson J. R. 1984, *MNRAS*, 210, 515
 Borriello A., Salucci P., Danese L., 2003, *MNRAS*, 341, 1109
 Boylan-Kolchin M., Ma C. -P., Quataert E., 2005, *MNRAS*, 362, 184
 Bryan G. L., Norman M. L., 1998, *ApJ*, 495, 80
 Bullock+01Bullock J. S., Kolatt T. S., Sigad Y., Somerville R. S., Kravtsov A. V., Klypin A. A., Primack J. R., Dekel A., 2001, *MNRAS*, 321, 559
 Busarello G., Capaccioli M., Capozziello S., Longo G., Puddu E., 1997, *A&A*, 320, 415
 Caon N., Capaccioli M., D’Onofrio M., 1993, *MNRAS*, 265, 1013
 Capelato H. V., de Carvalho R. R., Carlberg R. G., 1995, *ApJ*, 451, 525
 Cappellari M. et al., 2006, *MNRAS*, 366, 1126
 Cattaneo A., Dekel A., Devriendt J., Guiderdoni B., Blaizot J., 2006, *MNRAS*, 370, 1651
 Ciotti L., Lanzoni B., Renzini A., 1996, *MNRAS*, 282, 1
 Conselice C. J., Blackburne J. A., Papovich C., 2005, *ApJ*, 620, 564
 Couchman H. M. P., 1991, *ApJ*, 368, L23
 Cowie L. L., Songaila A., Hu E. M., Cohen J. G., 1996, *AJ*, 112, 839
 Dalcanton J., Spergel D. N., Summers F. J., 1997, *ApJ*, 482, 659
 Dantas C.C. et al., 2003, *MNRAS*, 340, 398
 Dekel A., Birnboim Y., 2006, *MNRAS*, 368, 2
 Dekel A., Stoehr F., Mamon G. A., Cox T. J., Primack J. R., 2005, *Nature*, 437, 707
 de Lucia G., Springel V., White S. D. M., Croton D., Kauffmann G., 2006, *MNRAS*, 366, 499
 de Vaucouleurs G., 1948, *Annales d’Astrophysique*, 11, 247
 de Zeeuw T., Franx M., 1991, *A.R.A.A.* 29, 239
 de Zeeuw P. T. et al., 2002, *MNRAS*, 329, 513
 Djorgovski S., Davis M., 1987, *ApJ*, 313, 59
 Domínguez-Tenreiro R., Sáiz A., Serna A., 2004, *ApJ*, 611, L5 (DSS04)
 Domínguez-Tenreiro R., Oñorbe J., Sáiz A., Artal H., Serna A., 2006, *ApJ*, 636, L77 (DTal06)
 D’Onofrio M., 2001, *MNRAS*, 326, 1517
 Douglas N. et al., 2002, *PASP*, 114, 1234
 Dressler A., Lynden-Bell D., Burstein D., Davies R. L., Faber S. M., Terlevich R., Wegner G., 1987, *ApJ*, 313, 42
 Elmegreen B., 2002, *ApJ*, 577, 206
 Evrard A., Silk J., Szalay A. S., 1990, *ApJ*, 365, 13

- Faber S. M., Dressler A., Davies R. L., Burstein D., Lynden-Bell D., 1987, in *Nearly Normal Galaxies. From the Planck Time to the Present*, ed. S. M. Faber, 175–183
- Faber S. M. et al., 2005, astro-ph/0506044 preprint
- Gerhard O., Kronawitter A., Saglia R. P., Bender R., 2001, 121, 1936
- Gnedin O. Y., Kravtsov A. V., Klypin A. A., Nagai D., 2004, ApJ, 616, 16
- González-García A. C., van Albada T. S., 2003, MNRAS, 342, 36
- González-García A. C., Balcells M., Olshevsky V. S., 2006, MNRAS, 372, 78
- Graham A. W., 1998, MNRAS, 295, 933
- Graham A., Colless M., 1997, MNRAS, 287, 221
- Guzik J., Seljak U., 2002, MNRAS, 335, 311
- Guzmán, R., Lucey, J., Bower, R. G. 1993, MNRAS, 265, 731
- Hernquist L., 1990, ApJ, 356, 359
- Hoekstra H., Yee H. K., Gladders M. D., 2004, ApJ, 606, 67
- Humphrey P. J., Buote D. A., Gastaldello F., Zappacosta L., Bullock J. S., Brighenti F., Mathews W. G., 2006, preprint astro-ph/0601301
- Jing Y. P., Suto Y., 2000, ApJ, 529, L69
- Katz N., 1992, ApJ, 391, 502
- Kauffmann G. et al., 2003, MNRAS, 341, 54
- Kennicutt R., 1998, ApJ, 498, 541
- Keres D., Katz N., Weinberg D. H., Davé, R., 2005, MNRAS, 363, 2
- Khochfar S., Burkert A., 2005, MNRAS, 359, 1379
- Kobayashi C., 2005, MNRAS, 361, 1216
- Koopmans L. V. E., Treu T., 2003, ApJ, 583, 606
- Koopmans L. V. E., Treu T., Bolton A. S., Burles S., Moustakas L. A., 2006, ApJ, 649, 599
- Kronawitter A., Saglia R. P., Gerhard O., Bender R., 2000, A&As, 144, 53
- Lima Neto G. B., Gerbal D., Márquez I. 1999, MNRAS, 309, 481
- Loewenstein M., 2000, ApJ, 532, 17
- Magorrian J., Ballantyne D., 2001, MNRAS, 322, 702
- Mamon G. A., Lokas E. L., 2005a, MNRAS, 362, 95
- Mamon G. A., Lokas E. L., 2005b, MNRAS, 363, 705
- Manrique A., Raig A., Salvador-Solé E., Sanchis T., Solanes J. M., 2003, ApJ, 593, 26
- Márquez I., Lima Neto G. B., Capelato H., Durret F., Gerbal D., 2000, A&A, 353, 873
- Meza A., et al., 2003, ApJ, 590, 619
- Moore B., Quinn T., Governato F., Stadel J., Lake G., 1999, MNRAS, 310, 1147
- Myers S. T., et al., 1995, ApJ, 447, L5
- Naab T., Burkert A., 2003, ApJ, 597, 893
- Naab T., Johansson P. H., Efstathiou G., & Ostriker J. P., 2005, astro-ph/0512235 preprint
- Naab T., Khochfar S., Burkert A., 2006, ApJ, 636L, 81
- Naab T., Trujillo I., 2006, MNRAS, 369, 625
- Napolitano N. R., et al., 2005, MNRAS, 357, 691
- Navarro J. F., Frenk C. S., White S. D. M., 1995, MNRAS, 275, 720
- Navarro J. F., Frenk C. S., White S. D. M. 1996, ApJ, 462, 563
- Navarro J. F., Hayashi E., Power C., Jenkins A. R., Frenk C. S., White S. D. M., Springel V., Stadel J., Quinn T. R., 2004, MNRAS, 349, 1039
- Nipoti C., Londrillo P., Ciotti L., 2003, MNRAS, 342, 501
- Oñorbe J., Domínguez-Tenreiro R., Sáiz A., Serna A., Artal H., 2005, ApJ, 632, L57
- Oñorbe J., Domínguez-Tenreiro R., Sáiz A., Artal H., Serna A., 2006, MNRAS, in press
- O’Sullivan E., Ponman T. J., 2004a, MNRAS, 349, 535
- O’Sullivan E., Ponman T. J., 2004b, MNRAS, 354, 935
- Padmanabhan N. et al., 2004, New Astronomy, 9, 329
- Pahre M. A., de Carvalho R. R., Djorgovski S. G., 1998, AJ, 116, 1606
- Prugniel P., Simien F., 1997, A&A, 321, 111
- Robertson B. et al., 2006, ApJ, 641, 21
- Romanowsky A. J., Kochanek C. S., 2001, ApJ, 553, 722
- Romanowsky A. J., et al., 2003, Science, 301, 1696
- Romanowsky A. J., 2006, EAS, 20, 119
- Romeo A. D., Portinari L., Sommer-Larsen J., 2005, MNRAS, 361, 983
- Sáiz, A., Domínguez-Tenreiro, R., Tissera, P. B., Courteau, S. 2001, MNRAS, 325, 119
- Sáiz A., 2003, PhD thesis, Universidad Autónoma de Madrid, Spain
- Sáiz A., Domínguez-Tenreiro R., Serna A. 2003, Ap&SS, 284, 411
- Sáiz A., Domínguez-Tenreiro R., Serna A. 2004, ApJ, 601, L131
- Salvador-Solé E., Manrique A., Solanes J. M. 2005, MNRAS, 358, 901
- Sarson G. R., Shukurov A., Nordlund A., Gudiksen B., Brandenburg A. 2004, Ap&SS, 292, 267
- Serna A., Domínguez-Tenreiro R., Sáiz A., 2003, ApJ, 597, 878
- Sérsic J. L., 1968, Atlas de galaxias australes (Córdoba, Argentina: Observatorio Astronómico, 1968)
- Sierra-Glez. de Buitrago M. M., Domínguez-Tenreiro R., Serna A., 2003, in *Highlights of Spanish Astronomy III*, p. 171, eds. J. Gallego et al. (Kluwer Ac. Press)
- Spiegel D. N., et al., 2006, astro-ph/0603449 preprint

- Sommer-Larsen J., Gotz M., Portinari L., 2002, *Ap&SS*, 281, 519
 Thomas D., Greggio L., Bender R., 1999, *MNRAS*, 302, 537
 Tissera P. B., Domínguez-Tenreiro R., 1998, *MNRAS*, 297, 177
 Tissera P. B., Lambas D. G., Abadi M. G. 1997, *MNRAS*, 286, 384
 Treu T., Koopmans L. V. E., 2004, *ApJ*, 611, 739
 Trujillo I., Graham A. W., Caon N., 2001, *MNRAS*, 326, 869
 Tucker W. H., 1975, *Radiation Precesses in Astrophysics* (New York, Wiley)
 van den Bosch F. C., Norberg P., Mo H. J., Yang X., 2004, *MNRAS*, 352, 1302
 Vazdekis A., Trujillo I., Yamada Y., 2004, *ApJ*, 601, L36
 Vázquez-Semadeni E., 2004a, *IAUS*, 221, 51
 Vázquez-Semadeni E., 2004b, *Ap&SS*, 292, 187
 Vergassola M., Dubrulle B., Frisch U., Noullez A., 1994, *A&A*, 289, 325
 van der Marel R. P., Franx M. 1993, *ApJ*, 407, 525
 Wechsler R. H., Bullock J. S., Primack J. R., Kravtsov A. V., Dekel A., 2002, *ApJ*, 568, 52
 Zhao D. H., Mo H. J., Jing Y. P., Borner G., 2003, *MNRAS*, 339, 12